
Neural Gaussian Radio Fields for Channel Estimation

Muhammad Ahmed Mohsin¹, Muhammad Umer¹, Ahsan Bilal², John Cioffi¹

¹Stanford University, ²University of Oklahoma

muahmed@stanford.edu, mumer@stanford.edu, ahsan.bilal-1@ou.edu, cioffi@stanford.edu

Abstract

Accurate channel state information (CSI) remains the most critical bottleneck in modern wireless networks, with pilot overhead consuming up to 11-21% of transmission bandwidth, increasing latency by 20-40% in massive MIMO systems, and reducing potential spectral efficiency by over 53%. Traditional estimation techniques fundamentally fail under mobility, with feedback delays as small as 4 ms causing 50% throughput degradation at even modest speeds (30 km/h). We present *neural Gaussian radio fields (nGRF)*, a novel framework that leverages explicit 3D Gaussian primitives to synthesize complex channel matrices accurately and efficiently. Unlike NeRF-based approaches that rely on slow implicit representations or existing Gaussian splatting methods that use non-physical 2D projections, nGRF performs direct 3D electromagnetic field aggregation, with each Gaussian acting as a localized radio modulator. nGRF demonstrates superior performance across diverse environments: in indoor scenarios, it achieves a 10.9 higher prediction SNR than state-of-the-art methods while reducing inference latency from 242 ms to just 1.1 ms (a 220 \times speedup). For large-scale outdoor environments, where existing approaches fail to function, nGRF achieves an SNR of 26.2 dB. Moreover, nGRF requires only 0.011 measurements/ft³ compared to 0.2-178.1 for existing methods, thereby reducing data collection burden by 18 \times . Training time is similarly reduced from hours to minutes (a 180 \times reduction), enabling rapid adaptation to dynamic environments. The code and datasets are available at <https://github.com/anonym-auth/n-grf>.

1 Introduction

Despite decades of work, real-time channel state information (CSI) *estimation and prediction* remains the principal unresolved bottleneck in both current and next-generation wireless networks. CSI, represented by the complex matrix \mathbf{H} , captures how signals propagate through direct paths, reflections, diffractions, and scattering between the transmitter and receiver. Accurate CSI enables transmitters to adapt their waveforms, power levels, and spatial precoding to channel conditions, directly determining achievable data rates and link reliability [1]. 5G and 6G networks aim for *sub-ms latencies and Gbps data rates that demand high-fidelity, low-overhead CSI estimation* [10].

Multiple-input multiple-output (MIMO) technology uses multiple antennas at the transmitter and receiver to send multiple parallel data streams over the same frequency band. This *spatial multiplexing* boosts data rates and capacity without extra bandwidth; with N antennas at each end, the theoretical peak throughput scales linearly by a factor of N . Massive MIMO further increases the antenna arrays by tens of folds, making \mathbf{H} difficult to characterize [2]. There are two fundamental reasons why *CSI estimation and prediction* remain unresolved. Firstly, pilot overhead in MIMO systems is significant, consuming 20% to 40% of each *coherence interval*. For instance, with a coherence time of 1 ms and a pilot duration of 0.2 ms, the overhead is 20%. If the coherence time drops to 0.5 ms while the pilot duration remains at 0.2 ms, the overhead increases to 40%, substantially decreasing throughput. Every extra pilot symbol diminishes the throughput available for data. For cell-free

massive MIMO systems, the feedback overhead of pilot symbols is estimated to be as large as 57 Gb/s [12]. A physical resource block (PRB) is the scheduling quantum used by 5G NR. In 3GPP Release-18 [15], it spans 12 consecutive sub-carriers over the full time extent of one slot (normally 14 OFDM symbols). Hence, a PRB contains $N_{\text{PRB}} = 12 \times 14 = 168$ resource elements in the $\mu = 1$ (30 kHz [sub-carrier spacing]) downlink grid. This count underlies the overhead fractions $18/168 \approx 11\%$ and $36/168 \approx 21\%$ of transmission bandwidth quoted earlier [6]. For current 3GPP systems, however, reducing pilots risks inaccurate CSI, which in turn lowers data throughput.

Secondly, even after channel information is acquired, it quickly becomes outdated in *dynamic environments* due to channel aging [28]. Under mobility, wireless channels decorrelate in milliseconds, so any delay between the CSI measurement and usage can render it outdated. For example, at a mid-band frequency around 3.5 GHz, a user moving at urban driving speeds (30 km/h) sees a channel coherence time of 2 ms [31]. A 4 ms feedback delay at 30 km/h can cut the data rate by $\approx 50\%$. A mmWave channel can decorrelate within a single 1 ms 5G subframe. Furthermore, dense networks face *pilot contamination*, where inter-cell pilot reuse degrades CSI accuracy, a bottleneck for MIMO [9].

AI-driven CSI estimators discussed in section 5 disregard the *physical 3D structure* governing radio propagation. Recent works exploring 3D Gaussian splatting (3DGS) [13] for wireless scene modeling are discussed in section 5. However, extant 3DGS models still regress only *scalar power, rely on low-capacity harmonic bases, and apply 2D projections* that fail to capture the full 3D electromagnetic fields. In this work, we propose *neural Gaussian radio fields (nGRF)*, a novel framework that uses an explicit volumetric scene representation based on 3D Gaussian primitives to synthesize complex channel matrices. By volumetrically aggregating 3D Gaussian primitives, nGRF renders complex-valued MIMO channels, outperforming both the slower implicit NeRF-based representations and 3DGS-based 2D-projected signal strength baselines. Each 3D Gaussian acts as a localized *radio modulator* whose properties are learned conditioned on the transmitter’s position. The channel at any receiver location is rendered as a spatially weighted Gaussian superposition. This physics-informed approach avoids abstract 2D projections, directly models electromagnetic field superposition in 3D, and offers dramatically faster channel estimation compared to implicit methods [32, 16].

Contributions. Our contributions are summarized as follows: We introduce nGRF, a framework that uses explicit 3D Gaussian primitives for MIMO channel matrix estimation. nGRF models electromagnetic field propagation through direct 3D aggregation instead of volumetric integration or 2D projections for physically accurate radio propagation modeling. Across diverse environments, nGRF achieves a 10.9 higher prediction SNR than state-of-the-art methods while supporting both SISO and MIMO configurations. For 5G NR systems with 100 MHz carriers (273 PRBs), nGRF reduces pilot overhead from 4,914 resource elements (9.8 kbit with QPSK) to just 96 bits (3×32 -bit position floats), decreasing resource grid occupation from 11-21% to 0.2%—a $> 100\times$ reduction in signaling load. Our evaluation demonstrates that nGRF requires $18\times$ less measurement density (0.011 vs. 0.2-178.1 measurements/ ft^3), trains $180\times$ faster, and offers $220\times$ lower inference latency (1.1 ms vs. 242 ms) compared to NeRF-based alternatives, while maintaining equal or better modeling fidelity in both indoor and outdoor scenarios.

2 Neural Gaussian Radio Fields

2.1 Problem Description

To provide context for our discussion, we refer the reader to Appendix A for background on wireless signal propagation, MIMO channel estimation, and the fundamentals of 3DGS. Channel estimation fundamentally requires solving a discrete approximation of Maxwell’s equations in complex environments. For time-harmonic electromagnetic fields at frequency ω , the vector wave equation is expressed as $\nabla \times \nabla \times \mathbf{E}(\mathbf{r}) - k^2 \mathbf{E}(\mathbf{r}) = -j\omega\mu_0\mathbf{J}(\mathbf{r})$ where $\mathbf{E}(\mathbf{r})$ is the electric field, $k = \omega\sqrt{\mu\epsilon}$ is the wavenumber, and $\mathbf{J}(\mathbf{r})$ represents current sources. In principle, solving this equation with appropriate boundary conditions would yield perfect CSI. However, this approach is computationally intractable for realistic environments where materials, geometries, and boundary conditions are complex and often unknown.

Existing approaches make varying trade-offs to address this challenge due to the sub-wavelength resolution needed for accurate wave simulation. Ray tracing methods approximate solutions to Maxwell’s equations by assuming the asymptotic limit where wavelength $\lambda \rightarrow 0$, reducing the

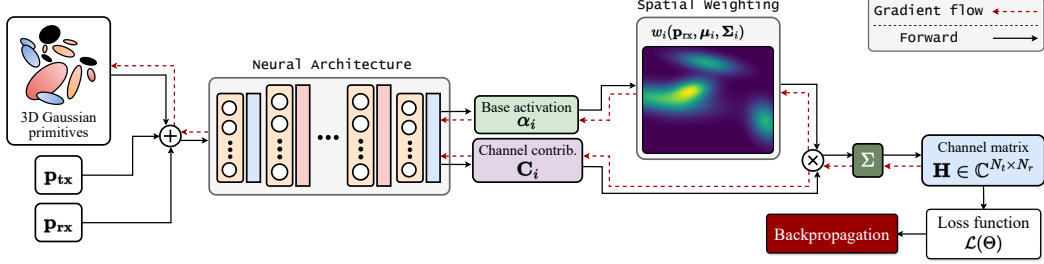


Figure 1: **An illustration of our nGRF framework.** The framework represents the wireless environment using a collection of 3D Gaussian primitives, each encoding localized electromagnetic field contributions.

problem to geometric optics. This approximation fails to capture important propagation effects like diffraction and becomes computationally prohibitive for complex scenes, scaling as $\mathcal{O}(N_{\text{ray}} N_s N_b^R)$, where N_{ray} is the number of rays, N_s is the number of surfaces, N_b is the average number of bounces, and R is the maximum reflection order.

Recent neural field approaches, particularly those based on NeRF [19], have attempted to learn implicit solutions to the wave equation. In these formulations, a volumetric field $F_\Theta : (\mathbf{x}, \mathbf{d}, \mathbf{p}_{\text{tx}}) \mapsto (\sigma, \mathbf{c})$ maps spatial coordinates $\mathbf{x} \in \mathbb{R}^3$, direction $\mathbf{d} \in \mathbb{S}^2$, and transmitter position $\mathbf{p}_{\text{tx}} \in \mathbb{R}^3$ to density $\sigma \in \mathbb{R}^+$ and complex-valued field contribution $\mathbf{c} \in \mathbb{C}^{N_t \times N_r}$. The channel response is then computed via numerical integration along rays as:

$$\mathbf{H}(\mathbf{p}_{\text{rx}}, \mathbf{p}_{\text{tx}}) = \sum_{i=1}^{N_{\text{rays}}} \sum_{j=1}^{N_{\text{samples}}} w_{i,j} \cdot F_\Theta(\mathbf{x}_{i,j}, \mathbf{d}_i, \mathbf{p}_{\text{tx}}), \quad (1)$$

where $w_{i,j}$ is a weighting function derived from the volumetric rendering equation.

While promising, such neural field approaches face architectural constraints: the need to represent the entire volumetric space using a fixed-resolution grid, requiring learning of $\mathcal{O}((\ell/\delta)^3)$ voxel attributes [35], where ℓ is the environment's characteristic length and $\delta \approx \lambda/8$ is the grid resolution; and the computational cost of querying a large MLP with $|\Theta| \approx 10^5 - 10^6$ parameters at $N_{\text{rays}} \times N_{\text{samples}} \approx 10^4 - 10^5$ points during inference.

A key insight driving our approach is that the electromagnetic field in a scene exhibits a spatially sparse structure dominated by discrete scatterers, reflectors, and diffractive elements. The field can be decomposed into a superposition of contributions from these elements, which can be efficiently modeled using anisotropic 3D Gaussian distributions. Mathematically, we propose to represent the field as:

$$\mathbf{E}(\mathbf{r}) \approx \sum_{i=1}^N \mathbf{E}_i(\mathbf{r}) = \sum_{i=1}^N \mathbf{A}_i G_i(\mathbf{r}; \boldsymbol{\mu}_i, \boldsymbol{\Sigma}_i), \quad (2)$$

where $\mathbf{E}_i(\mathbf{r})$ is the contribution from the i -th element, \mathbf{A}_i is a complex amplitude tensor, and $G_i(\mathbf{r}; \boldsymbol{\mu}_i, \boldsymbol{\Sigma}_i)$ is a 3D Gaussian distribution with mean $\boldsymbol{\mu}_i$ and covariance $\boldsymbol{\Sigma}_i$.

Representation via 3D Gaussian primitives delivers significant benefits in computational efficiency, data requirements, and inference latency. Our approach reduces measurement density requirements to $\rho_{\text{data}} \approx 0.011$ measurements/ft³, training time to $\tau_{\text{train}} \approx 2$ minutes, and inference latency to $\tau_{\text{infer}} \approx 1.1$ ms, while maintaining better modeling fidelity (see Figure 4). This reduction in computational demands and data requirements makes real-time channel estimation feasible for time-critical applications in next-generation wireless systems.

2.2 nGRF Design

nGRF represents an electromagnetic environment as a collection of N anisotropic 3D Gaussian elements $\{G_i\}_{i=1}^N$, each parameterized by a mean position $\boldsymbol{\mu}_i \in \mathbb{R}^3$, a covariance matrix $\boldsymbol{\Sigma}_i \in \mathbb{R}^{3 \times 3}$, and electromagnetic attributes derived from neural networks. Figure 1 illustrates the overall architecture of our nGRF framework.

The principle of our approach is the linearity of Maxwell’s equations in non-magnetic media, which allows us to decompose the total electromagnetic field into a superposition of contributions from individual field elements. Each Gaussian primitive in our model corresponds to a localized field contribution, with its spatial extent and orientation serving as adaptive basis functions that model the spatial variation of the electromagnetic field. These Gaussians are optimized to capture complex wave phenomena rather than directly representing geometric properties of physical scatterers in the environment.

For a given 3D point $\mathbf{x} \in \mathbb{R}^3$, the probability density function of the i -th Gaussian is given by

$$G_i(\mathbf{x}) = \frac{1}{(2\pi)^{3/2}|\Sigma_i|^{1/2}} \exp\left(-\frac{1}{2}(\mathbf{x} - \boldsymbol{\mu}_i)^T \Sigma_i^{-1}(\mathbf{x} - \boldsymbol{\mu}_i)\right), \quad (3)$$

where $|\Sigma_i|$ is the determinant of the covariance matrix. In practice, we normalize this function and only use the exponential term as our weighting function.

The covariance matrix Σ_i must be positive semi-definite to represent a valid Gaussian distribution. To ensure this constraint while enabling differentiable optimization, we parameterize it using a rotation-scaling decomposition $\Sigma_i = \mathbf{R}_i \mathbf{S}_i^2 \mathbf{R}_i^T$ where $\mathbf{R}_i \in \text{SO}(3)$ is a rotation matrix and $\mathbf{S}_i = \text{diag}(s_{i,1}, s_{i,2}, s_{i,3})$ is a diagonal scaling matrix with $s_{i,j} > 0$. The rotation matrix \mathbf{R}_i is parameterized using a unit quaternion $\mathbf{q}_i = [q_{i,w}, q_{i,x}, q_{i,y}, q_{i,z}]^T$ with $\|\mathbf{q}_i\|_2 = 1$, which maps to $\text{SO}(3)$ via the Rodrigues’ rotation formula (Eq. 22 of Appendix C), whereas the scaling parameters $s_{i,j}$ are parameterized through an exponential mapping $s_{i,j} = \exp(s'_{i,j})$ with $s'_{i,j} \in \mathbb{R}$, ensuring positivity while allowing unconstrained optimization.

For a MIMO system with N_t transmit antennas and N_r receive antennas, the channel matrix $\mathbf{H} \in \mathbb{C}^{N_t \times N_r}$ represents the complex-valued gains between each transmit-receive antenna pair. Our model computes this matrix by aggregating contributions from all Gaussian elements, weighted by their influence at the receiver position (as detailed in Section 2.4). For each receiver position $\mathbf{p}_{\text{rx}} \in \mathbb{R}^3$ and transmitter position $\mathbf{p}_{\text{tx}} \in \mathbb{R}^3$, spatial weighting functions w_i determine how each Gaussian element contributes to the final channel matrix, where \mathbf{z}_i is a latent feature vector derived from the attribute network, and $\mathbf{C}_i \in \mathbb{C}^{N_t \times N_r}$ is the complex-valued channel contribution matrix produced by the decoder network.

This formulation enables direct “rendering” of the channel matrix without ray marching or volumetric integration, resulting in faster inference times compared to existing approaches (see Section 3). The complexity of this computation is $\mathcal{O}(N N_t N_r)$, where N is the number of Gaussian elements, which is typically orders of magnitude smaller than the number of voxels in a fixed-resolution grid. For example, modeling an indoor space of $10\text{m} \times 10\text{m} \times 3\text{m}$ with a voxel resolution of $\lambda/8 \approx 0.006\text{m}$ would require $\approx 8.3 \times 10^7$ voxels, whereas our approach uses only $\approx 10^3$ Gaussian primitives.

2.3 Attribute and Decoder Networks

The electromagnetic properties of each Gaussian element are determined through a neural network that transforms spatial information into complex-valued channel contributions. Our network design processes position information to generate appropriate electromagnetic attributes for each Gaussian primitive, allowing them to function as localized radio modulators that capture scattering phenomena in the environment. Effectively, each Gaussian models a spatial region where specific electromagnetic interactions occur. Figure 2 shows the architecture of our attribute and decoder networks.

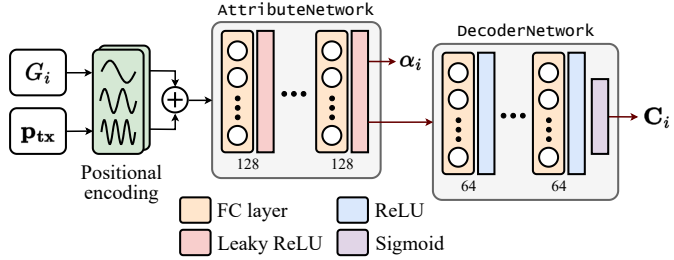


Figure 2: Neural architecture. The **AttributeNetwork** processes Gaussian and transmitter positions through separate positional encoders, processing them to produce latent features and base activation logits. The **DecoderNetwork** transforms latent features into complex channel contributions with normalized output values.

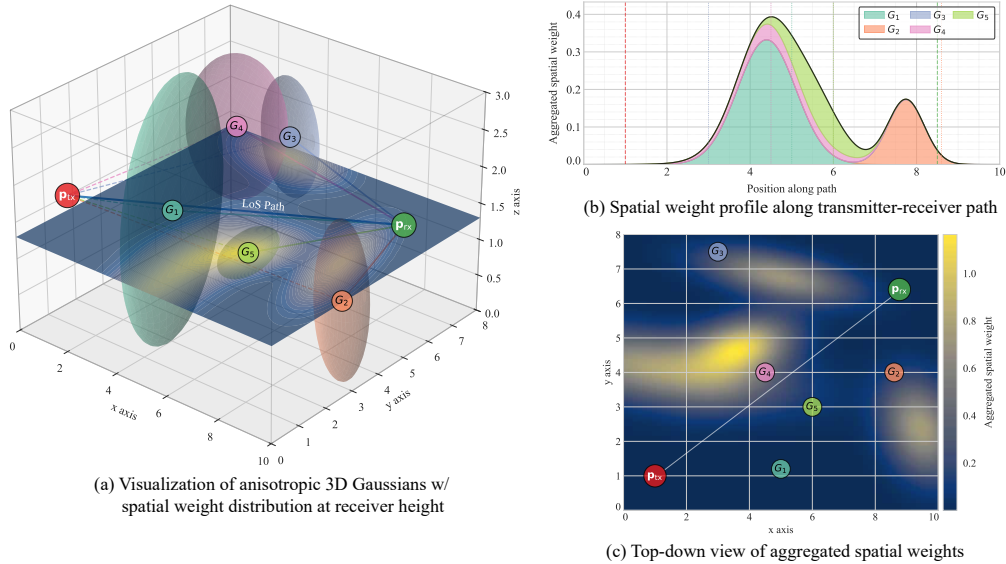


Figure 3: **Visualization of the spatial weighting in nGRF.** (a) Anisotropic 3D Gaussians (G_1 - G_5) are shown as ellipsoids with their shapes determined by covariance Σ_i , along with the transmitter (p_{tx}), receiver (p_{rx}), and line-of-sight path. The heat map represents the spatial weight distribution at receiver height. (b) Weight profile along the p_{tx} - p_{rx} path showing individual Gaussian contributions and their cumulative effect (black outline). (c) Top-down view of the aggregated spatial weights where brighter regions indicate stronger electromagnetic influence.

The attribute network $f_{\text{attr}} : \mathbb{R}^3 \times \mathbb{R}^3 \rightarrow \mathbb{R}^d \times \mathbb{R}$ maps the Gaussian position μ_i and transmitter position p_{tx} to a latent feature vector $\mathbf{z}_i \in \mathbb{R}^d$ and a base activation value $\alpha_i \in \mathbb{R}$: $\mathbf{z}_i, \alpha_i = f_{\text{attr}}(\mu_i, p_{tx}; \Theta_{\text{attr}})$

To capture the high-frequency spatial variations inherent in electromagnetic fields, particularly those with wavelength $\lambda \ll \ell$ (where ℓ is the characteristic length of the environment), we apply a multi-resolution positional encoding to the input coordinates [19]:

$$\gamma_L(\mathbf{x}) = [\mathbf{x}, \sin(2^0 \pi \mathbf{x}), \cos(2^0 \pi \mathbf{x}), \dots, \sin(2^{L-1} \pi \mathbf{x}), \cos(2^{L-1} \pi \mathbf{x})], \quad (4)$$

where L is the number of frequency bands; positional encoding transforms the input coordinates into a higher-dimensional space where the network can more easily learn high-frequency functions. Given that the wavelengths of electromagnetic waves are typically in the range of centimeters to millimeters, it becomes particularly necessary for modeling the spatial variations of the electromagnetic field. As in Appendix F, we find that to represent spatial variations at the scale of $\lambda/2$, which is the Nyquist limit for sampling electromagnetic fields, the frequency encoding should satisfy $2^{L-1} \geq \ell/\lambda$. For our experimental setup with $\ell \approx 50$ m and $\lambda \approx 0.05$ m, we choose $L = 16$.

The per-Gaussian latents \mathbf{z}_i capture the electromagnetic characteristics localized to the Gaussian element, while the base activation value α_i determines its “overall” strength and allows separate optimization of field magnitude and complex properties (e.g., phase, polarization) for effective modeling of wave superposition effects. Then, the decoder network $f_{\text{dec}} : \mathbb{R}^d \rightarrow \mathbb{C}^{N_t \times N_r}$ maps \mathbf{z}_i to the complex channel contribution vector \mathbf{C}_i . Since neural networks can only output real values, we parameterize the complex vector using separate real and imaginary components: $\mathbf{C}_i = \mathbf{C}_i^{\text{re}} + j\mathbf{C}_i^{\text{im}}$.

2.4 Channel Rendering

The channel rendering process directly computes the MIMO channel matrix through a weighted summation of Gaussian contributions, eliminating the computational overhead of ray marching or volumetric integration. Existing approaches usually require $\mathcal{O}(N_{\text{ray}} N_{\text{samples}} |\Theta|)$ operations with expensive per-sample MLP evaluations, while our method’s $\mathcal{O}(N N_t N_r)$ complexity utilizes the sparsity of radio propagation environments. Figure 3 illustrates this spatial weighting mechanism.

For a receiver at position $\mathbf{p}_{rx} \in \mathbb{R}^3$ and a transmitter at position $\mathbf{p}_{tx} \in \mathbb{R}^3$, the MIMO channel matrix $\mathbf{H}(\mathbf{p}_{rx}, \mathbf{p}_{tx}) \in \mathbb{C}^{N_t \times N_r}$ is computed as a spatially-weighted superposition of electromagnetic field

contributions, following the principle of superposition that governs Maxwell's equations in linear media:

$$\mathbf{H}(\mathbf{p}_{\text{rx}}, \mathbf{p}_{\text{tx}}) = \sum_{i=1}^N w_i(\mathbf{p}_{\text{rx}}, \boldsymbol{\mu}_i, \boldsymbol{\Sigma}_i) \cdot \mathbf{C}_i \quad (5)$$

The spatial weight w_i determines how much each Gaussian element contributes to the received signal and is derived from the Gaussian probability density function:

$$w_i(\mathbf{p}_{\text{rx}}, \boldsymbol{\mu}_i, \boldsymbol{\Sigma}_i) = \alpha_i \cdot \exp\left(-\frac{1}{2}(\mathbf{p}_{\text{rx}} - \boldsymbol{\mu}_i)^T \boldsymbol{\Sigma}_i^{-1} (\mathbf{p}_{\text{rx}} - \boldsymbol{\mu}_i)\right) \quad (6)$$

where α_i is the base activation of the Gaussian element, and $\boldsymbol{\Sigma}_i^{-1}$ is the precision matrix. This formulation has a clear physical interpretation: the contribution of each element decreases with the Mahalanobis distance from the receiver to the Gaussian center, reflecting the spatial decay of electromagnetic influence.

Unlike 3DGS-based methods that project 3D Gaussians onto 2D image planes via rasterization, such approaches cannot meaningfully represent electromagnetic propagation that occurs in true 3D space rather than on projection surfaces. Adapting 3DGS would require artificial mapping of channel responses onto arbitrary projection geometries, introducing non-physical transformations and distortions. Instead, we directly evaluate the electromagnetic field at receiver locations using physics-informed weighting functions. Algorithm 1 summarizes our approach. For the definition of `build_rotation` and `build_covariance_inverse` functions, please refer to Appendix C.

Algorithm 1: nGRF Channel Rendering

Require : Gaussian parameters $\{\boldsymbol{\mu}_i, \mathbf{s}_i, \mathbf{q}_i, \mathbf{z}_i, \alpha_i\}_{i=1}^N$, transmitter pos. \mathbf{p}_{tx} , receiver pos. \mathbf{p}_{rx}
Ensure : Channel matrix $\mathbf{H}(\mathbf{p}_{\text{rx}}, \mathbf{p}_{\text{tx}})$

```

1  $\mathbf{H} \leftarrow \mathbf{0} \in \mathbb{C}^{N_t \times N_r}$ 
2 for  $i \leftarrow 1$  to  $N$  do
3    $\mathbf{R}_i \leftarrow \text{build\_rotation}(\mathbf{q}_i)$ 
4    $\boldsymbol{\Sigma}_i^{-1} \leftarrow \text{build\_covariance\_inverse}(\mathbf{R}_i, \mathbf{s}_i)$ 
5    $\mathbf{d}_i \leftarrow \mathbf{p}_{\text{rx}} - \boldsymbol{\mu}_i$ 
6    $w_i \leftarrow \alpha_i \exp(-\frac{1}{2} \mathbf{d}_i^T \boldsymbol{\Sigma}_i^{-1} \mathbf{d}_i)$ 
7    $\mathbf{C}_i \leftarrow f_{\text{dec}}(\mathbf{z}_i)$ 
8    $\mathbf{H} \leftarrow \mathbf{H} + w_i \cdot \mathbf{C}_i$ 
9 Return  $\mathbf{H}$ 

```

2.5 Convergence

Unlike implicit neural fields that optimize millions of parameters to approximate continuous volumetric functions, nGRF's explicit Gaussian primitives provide a structural inductive bias aligned with electromagnetic scattering physics. This section describes our loss function formulation and optimization strategy, which enables rapid training of our model.

The loss function $\mathcal{L}(\Theta)$ combines channel estimation error with regularization terms: $\mathcal{L}(\Theta) = \mathcal{L}_{\text{est}} + \lambda_{\text{act}} \mathcal{L}_{\text{activation}} + \lambda_{\text{reg}} \mathcal{L}_{\text{regularization}}$. Here, \mathcal{L}_{est} measures the prediction error between the estimated and ground-truth channel matrices using a complex-valued mean squared error:

$$\mathcal{L}_{\text{est}} = \frac{1}{|B|} \sum_{b \in B} \|\mathbf{H}_{\text{pred}}^{(b)} - \mathbf{H}_{\text{gt}}^{(b)}\|_F^2 \quad (7)$$

where B is the mini-batch, $\mathbf{H}_{\text{pred}}^{(b)}$ and $\mathbf{H}_{\text{gt}}^{(b)}$ are the predicted and ground-truth channel matrices for sample b , and $\|\cdot\|_F$ is the Frobenius norm. The activation loss $\mathcal{L}_{\text{activation}}$ is an L1 penalty on the base activations to encourage sparsity in the model:

$$\mathcal{L}_{\text{activation}} = \frac{1}{N} \sum_{i=1}^N |\alpha_i| \quad (8)$$

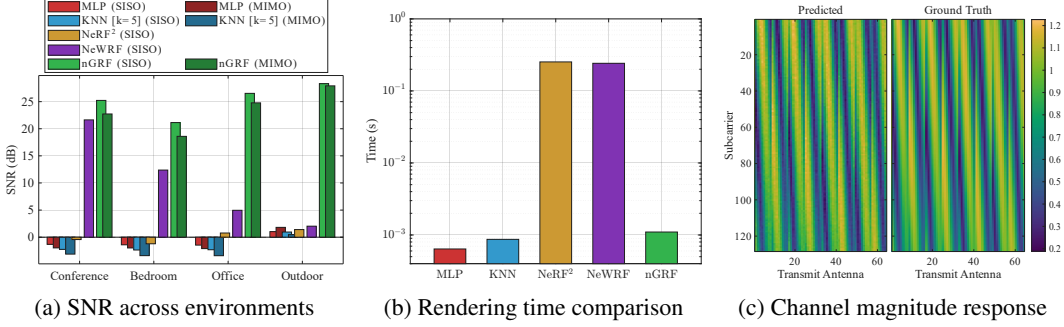


Figure 4: **Performance evaluation of nGRF.** (a) SNR performance across different environments shows nGRF consistently outperforming other methods, particularly in complex scenarios. (b) Inference time comparison showing speedups of nGRF over NeRF-based approaches. (c) Comparison between predicted (left) and ground-truth (right) channel magnitude response across subcarriers and transmit antennas in the outdoor environment.

where α_i is the base activation of the i -th Gaussian element. Moreover, the regularization loss $\mathcal{L}_{\text{regularization}}$ prevents degenerate Gaussian shapes by constraining the scaling parameters:

$$\mathcal{L}_{\text{regularization}} = \frac{1}{N} \sum_{i=1}^N \sum_{j=1}^3 \max(0, s_{i,j_{\min}} - s_{i,j}) + \max(0, s_{i,j} - s_{i,j_{\max}}) \quad (9)$$

where $s_{i,j}$ is the j -th scaling parameter of the i -th Gaussian, and $s_{i,j_{\min}}$ and $s_{i,j_{\max}}$ are the minimum and maximum allowed values.

For a model with parameters $\Theta = \{\boldsymbol{\mu}_i, \mathbf{q}_i, \mathbf{s}_i\}_{i=1}^N \cup \{\Theta_{\text{attr}}, \Theta_{\text{decoder}}\}$, we minimize the loss function using stochastic gradient descent with parameter-specific learning rate schedules: $\Theta^{(j+1)} = \Theta^{(j)} - \boldsymbol{\eta}^{(j)} \odot \nabla_{\Theta} \mathcal{L}(\Theta^{(j)})$ where $\boldsymbol{\eta}^{(j)}$ is a vector of learning rates for each parameter group at iteration j , and \odot denotes element-wise multiplication.

3 Evaluation

Experimental Setup. We evaluate nGRF across diverse propagation environments to demonstrate its generalizability. For indoor scenarios, we use three distinctly different environments: a conference room, a bedroom, and an office space, while a large-scale residential area is used for the outdoor scenario. More details about the considered environments and dataset generation are explained in Appendix B.

For the antenna configurations, we employ a 4×4 uniform rectangular array (URA) as the transmitter and a 2-element uniform linear array (ULA) as the receiver for indoor scenarios. For the outdoor scenario, we scale up to an 8×8 ULA for the transmitter while maintaining the 2-element ULA for the receiver. We also configure SISO setups with omnidirectional antennas to enable a fair comparison with existing approaches that primarily support single-antenna configurations (NeRF² and NeWRF). For each environment, we generate a varying number of measurements/ft³ in accordance with the environment’s area. Moreover, we use 80% of samples for training and the remaining 20% for testing. All experiments are implemented in PyTorch 2.7.0 with CUDA 12.8 bindings and trained on a single NVIDIA RTX 5090 GPU with 32 GB of memory.

Results. We compare nGRF against several state-of-the-art and standard baselines: NeWRF [16], NeRF² [35], a standard multi-layer perceptron (MLP) network, and a k-nearest neighbors (KNN) approach. Figure 4 presents a comprehensive evaluation of these methods. We use signal-to-noise ratio (SNR) as the primary performance metric, which quantifies prediction accuracy and is defined as $\text{SNR} (\text{dB}) = 10 \log_{10}(|\mathbf{H}_{\text{gt}}|_F^2 / |\mathbf{H}_{\text{pred}} - \mathbf{H}_{\text{gt}}|_F^2)$.

As shown in Figure 4a, nGRF consistently outperforms all baselines across all environments. For indoor scenarios, nGRF achieves SNRs of 25.23 dB, 21.14 dB, and 26.53 dB for the conference room, bedroom, and office environments, respectively, in SISO configurations. For MIMO configurations, nGRF maintains strong performance with SNRs of 22.73 dB, 19.60 dB, and 24.78 dB across the

same environments. This represents, on average, a 10.9 dB improvement over the next best method (NeWRF) for indoor environments in SISO configurations. In the large-scale outdoor scenario, nGRF achieves SNR values of 28.32 dB for SISO and 27.92 dB for MIMO, while NeWRF and NeRF² struggle to model the expansive environment effectively, achieving 2.03 dB and 1.40 dB SNR, respectively. Traditional approaches like MLP and KNN understandably perform worse, with SNRs below 0 dB in most indoor environments.

Figure 4b compares the rendering time (inference latency) of different methods. nGRF achieves *220× speedup and requires 1.1 ms for channel estimation* compared to 242 ms for NeWRF and 253 ms for NeRF². While baseline approaches like MLP (0.64 ms) and KNN (0.87 ms) offer marginally faster inference, their significantly lower accuracy makes them unsuitable for practical deployment. Real-time channel estimation in dynamic wireless environments with coherence times as short as 2 ms demands both high accuracy and low latency, making nGRF the only viable solution.

Figure 4c shows the channel magnitude response across subcarriers and transmit antennas for a particular receive antenna in the outdoor environment. Despite being trained on a single carrier frequency, nGRF accurately predicts the channel response across all subcarriers. nGRF models electromagnetic field physics with 3D Gaussian primitives that capture spatial wave propagation and environmental interactions, yielding accurate, frequency-generalized CSI across all wideband OFDM subcarriers for robust system performance.

Table 1: **Ablation experiments for nGRF.** We evaluate performance variations across different numbers of Gaussians, optimization strategies, and initialization methods.

Configuration	SNR (dB)	Train Time (min)	Render Time (ms)
nGRF (baseline)	28.32	2.3	1.10
<i># of Gaussians</i>			
500	26.13	1.9	0.94
1,000	26.57	2.2	1.06
5,000	23.31	3.0	1.27
10,000	18.04	3.6	1.40
<i>Positions μ_i</i>			
Fixed means	4.11	2.3	1.10
<i>Initialization</i>			
LiDAR-based	19.76	2.3	1.10

Ablation Studies. We perform several ablation studies to understand the contribution of different components of nGRF. Table 1 summarizes the results for the outdoor environment.

1. *Number of Gaussians.* Reducing the number of Gaussians to 500 or 1000 maintains competitive performance. However, increasing this figure to 5000 or 10000 leads to severe degradation. The experiments in Table 1 indicate that while a minimum threshold of Gaussians is necessary to capture electromagnetic field complexity, excessive parameterization induces overfitting and diminishing returns.
2. *Gaussian Positions.* When we fix the positions of Gaussian primitives (making them non-trainable), the SNR drops from 28.32 dB to 4.11 dB. Optimizing the spatial distribution of Gaussians is crucial for accurately modeling the electromagnetic field to allow the model to adapt to the specific propagation characteristics of the environment.
3. *Initialization Strategy.* Contrary to intuition, initializing Gaussian means using a LiDAR-generated point cloud yields worse performance than random initialization. In nGRF, Gaussians function not as physical scatterers of radio waves but as adaptive basis functions for the radio propagation field. Consequently, geometry-constrained initialization restricts the model’s ability to capture complex wave phenomena that transcend environmental geometry.

Additional ablation studies examining the impact of hyperparameters, initialization, and measurement density are provided in Appendix F.

4 Limitations and Future Work

Despite nGRF’s advantages, it exhibits two notable **limitations**. First, the framework demonstrates significant hyperparameter sensitivity, particularly to Gaussian scaling parameters and initialization values; performance can degrade by up to 14.49 dB with suboptimal scaling initialization, with

similar sensitivity observed for learning rates and regularization coefficients. Second, the current formulation lacks mechanisms for handling time-varying channels in dynamic environments with mobile users. **Future work** will focus on developing robust hyperparameter selection through meta-learning approaches and extending nGRF to model temporal dynamics through time-dependent Gaussian attributes. Additionally, we plan to implement incremental update feedback mechanisms for channel update based on channel prediction error for real-time adaptation to mobility scenarios, enabling predictive channel estimation for high-velocity applications where coherence times approach the millisecond threshold.

5 Related Work

This section is divided into two parts. First, we discuss the NeRF-based approaches for channel estimation and why they fail to address the CSI problem, and then we discuss the 3D geometric-based understanding approaches.

NeRF-Based Approaches. NeRFs have been adapted from optical to radio frequency domains for channel estimation. NeRF² [35] introduced continuous volumetric RF scene representation using neural radiance fields, achieving 82% higher performance than baseline algorithms with their “turbo-learning” approach for synthetic data generation. NeWRF [16] developed a framework for radiation field reconstruction using sparse measurements and incorporated wireless propagation physics into NeRF’s optical framework. These approaches, however, face many practical limitations: they require prohibitively dense measurements (178.1 measurements/ft³ for NeRF²), impose substantial computational demands (several hours of training on high-end GPUs), and exhibit high inference latency (200–350 ms per estimation). Such constraints render them impractical for real-time applications requiring millisecond-level decisions, such as vehicular communications or dynamic network optimization. Furthermore, current implementations remain limited to SISO scenarios and thus leave the need for solutions applicable to MIMO systems unaddressed.

3DGS-Based Approaches. 3DGS offers faster rendering and explicit scene representation compared to NeRF-based methods. WRF-GS [32] models wireless radial fields using 3DGS with spherical harmonics for wireless feature embedding. However, it primarily targets spatial spectrum reconstruction rather than complex channel matrices and relies on the Mercator projection, which inadequately represents electromagnetic propagation physics. Moreover, its optimization process requires as many as 600,000 steps for convergence. RadSplatter [21] extends 3DGS for wireless radiomap extrapolation using a relaxed-mean reparameterization scheme, but this introduces potential instability in the optimization process (due to gradient discontinuities at relaxation boundaries). While achieving high extrapolation accuracy, its focus on signal strength (RSSI) rather than complex-valued MIMO channels limits its utility for channel estimation. RFSPM [33] addresses fidelity-scalability trade-offs with domain-specific adaptations, including gradient-guided attribute learning and RF-customized CUDA kernels, but these additions increase implementation complexity (e.g. small MLP per Gaussian) without justifiable benefits. Fundamentally, these approaches rely on limited-capacity representations and splatting (designed for optical signals) techniques that inadequately model the 3D nature of electromagnetic wave propagation, applying view-dependent projections instead of directly capturing signal superposition in three-dimensional space.

6 Conclusion and Broader Impact

This work introduced nGRF, a framework that synthesizes complex MIMO channel matrices by directly aggregating explicit 3D Gaussian primitives, each acting as a learned radio modulator. nGRF achieves state-of-the-art channel estimation accuracy with major reductions in latency, training time, and data requirements, overcoming key limitations of prior implicit and projection-based methods. The core contribution lies in demonstrating that structured, explicit representations, informed by physical principles, can provide a more powerful and efficient inductive bias for modeling complex field phenomena than generic deep learning architectures. Beyond wireless, the principles demonstrated in nGRF offer a blueprint for developing efficient, primitive-based neural field models in other scientific and engineering domains where capturing complex 3D interactions is necessary, thereby potentially accelerating discovery and reducing the carbon footprint of large-scale AI by enabling more sample- and computationally-efficient modeling.

References

- [1] Haowei Bai and Mohammed Atiquzzaman. Error modeling schemes for fading channels in wireless communications: A survey. *IEEE Communications Surveys & Tutorials*, 5(2):2–9, 2003.
- [2] Eren Balevi, Akash Doshi, and Jeffrey G Andrews. Massive mimo channel estimation with an untrained deep neural network. *IEEE Transactions on Wireless Communications*, 19(3):2079–2090, 2020.
- [3] Jonathan T Barron, Ben Mildenhall, Matthew Tancik, Peter Hedman, Ricardo Martin-Brualla, and Pratul P Srinivasan. Mip-nerf: A multiscale representation for anti-aliasing neural radiance fields. In *Proceedings of the IEEE/CVF international conference on computer vision*, pages 5855–5864, 2021.
- [4] Xiang Cheng, Cheng-Xiang Wang, David I Laurenson, Sana Salous, and Athanasios V Vasilakos. An adaptive geometry-based stochastic model for non-isotropic mimo mobile-to-mobile channels. *IEEE transactions on wireless communications*, 8(9):4824–4835, 2009.
- [5] Dan Crisu, Sorin Cotofana, Stamatis Vassiliadis, and Petri Luuha. Efficient hardware for tile-based rasterization. In *Proceedings of 15th Annual Workshop on Circuits, Systems, and Signal Processing (ProRISC 2004)*, pages 352–357, 2004.
- [6] Erik Dahlman, Gunnar Mildh, Stefan Parkvall, Janne Peisa, Joachim Sachs, and Yngve Selén. 5g radio access. *Ericsson review*, 6(1), 2014.
- [7] Chuong B Do. The multivariate gaussian distribution. *Section Notes, Lecture on Machine Learning, CS*, 229, 2008.
- [8] Dean G Duffy. *Green's functions with applications*. Chapman and Hall/CRC, 2015.
- [9] Olakunle Elijah, Chee Yen Leow, Tharek Abdul Rahman, Solomon Nunoo, and Solomon Zakwoi Iliya. A comprehensive survey of pilot contamination in massive mimo—5g system. *IEEE Communications Surveys & Tutorials*, 18(2):905–923, 2015.
- [10] Marco Giordani, Michele Polese, Marco Mezzavilla, Sundeep Rangan, and Michele Zorzi. Toward 6g networks: Use cases and technologies. *IEEE Communications Magazine*, 58(3):55–61, 2020.
- [11] Andrea Goldsmith. *Wireless communications*. Cambridge university press, 2005.
- [12] Amit P Jardosh, Krishna N Ramachandran, Kevin C Almeroth, and Elizabeth M Belding-Royer. Understanding congestion in ieee 802.11 b wireless networks. In *Proceedings of the 5th ACM SIGCOMM conference on Internet Measurement*, pages 25–25, 2005.
- [13] Bernhard Kerbl, Georgios Kopanas, Thomas Leimkühler, and George Drettakis. 3d gaussian splatting for real-time radiance field rendering, 2023. URL <https://arxiv.org/abs/2308.04079>.
- [14] Farzad Khorasani, Hodjat Asghari Esfeden, Amin Farmahini-Farahani, Nuwan Jayasena, and Vivek Sarkar. Regmutex: Inter-warp gpu register time-sharing. In *2018 ACM/IEEE 45th Annual International Symposium on Computer Architecture (ISCA)*, pages 816–828. IEEE, 2018.
- [15] Xingqin Lin. An overview of 5g advanced evolution in 3gpp release 18. *IEEE Communications Standards Magazine*, 6(3):77–83, 2022.
- [16] Haofan Lu, Christopher Vattheuer, Baharan Mirzasoleiman, and Omid Abari. Newrf: A deep learning framework for wireless radiation field reconstruction and channel prediction, 2024. URL <https://arxiv.org/abs/2403.03241>.
- [17] Roger C Lyndon. Properties preserved under homomorphism. 1959.
- [18] Goeffrey J McLachlan. Mahalanobis distance. *Resonance*, 4(6):20–26, 1999.

[19] Ben Mildenhall, Pratul P. Srinivasan, Matthew Tancik, Jonathan T. Barron, Ravi Ramamoorthi, and Ren Ng. Nerf: Representing scenes as neural radiance fields for view synthesis, 2020. URL <https://arxiv.org/abs/2003.08934>.

[20] David Neumann, Thomas Wiese, and Wolfgang Utschick. Learning the mmse channel estimator. *IEEE Transactions on Signal Processing*, 66(11):2905–2917, 2018.

[21] Michael Niemeyer, Fabian Manhardt, Marie-Julie Rakotosaona, Michael Oechsle, Daniel Duckworth, Rama Gosula, Keisuke Tateno, John Bates, Dominik Kaeser, and Federico Tombari. Radsplat: Radiance field-informed gaussian splatting for robust real-time rendering with 900+ fps, 2025. URL <https://arxiv.org/abs/2403.13806>.

[22] G.G. Raleigh and J.M. Cioffi. Spatio-temporal coding for wireless communication. *IEEE Transactions on Communications*, 46(3):357–366, 1998. doi: 10.1109/26.662641.

[23] Theodore S. Rappaport, Shu Sun, Rimma Mayzus, Hang Zhao, Yaniv Azar, Kevin Wang, George N. Wong, Jocelyn K. Schulz, Mathew Samimi, and Felix Gutierrez. Millimeter wave mobile communications for 5g cellular: It will work! *IEEE Access*, 1:335–349, 2013. doi: 10.1109/ACCESS.2013.2260813.

[24] Alejandro Ribeiro, Ioannis D Schizas, Stergios I Roumeliotis, and Georgios Giannakis. Kalman filtering in wireless sensor networks. *IEEE Control Systems Magazine*, 30(2):66–86, 2010.

[25] Jack Salz and Jack H Winters. Effect of fading correlation on adaptive arrays in digital mobile radio. *IEEE transactions on Vehicular Technology*, 43(4):1049–1057, 2002.

[26] Bernard Sklar. Rayleigh fading channels in mobile digital communication systems. i. characterization. *IEEE Communications magazine*, 35(7):90–100, 1997.

[27] Peter Sturm. Pinhole camera model. In *Computer Vision: A Reference Guide*, pages 983–986. Springer, 2021.

[28] Kien T Truong and Robert W Heath. Effects of channel aging in massive mimo systems. *Journal of Communications and Networks*, 15(4):338–351, 2013.

[29] Saeed V Vaseghi and Saeed V Vaseghi. Wiener filters. *Advanced Signal Processing and Digital Noise Reduction*, pages 140–163, 1996.

[30] Michael Wand, Matthias Fischer, Ingmar Peter, Friedhelm Meyer auf der Heide, and Wolfgang Straßer. The randomized z-buffer algorithm: Interactive rendering of highly complex scenes. In *Proceedings of the 28th annual conference on Computer graphics and interactive techniques*, pages 361–370, 2001.

[31] Yafei Wang, Xinpeng Yi, Hongwei Hou, Wenjin Wang, and Shi Jin. Robust symbol-level precoding for massive mimo communication under channel aging. *IEEE Transactions on Wireless Communications*, 2024.

[32] Chaozheng Wen, Jingwen Tong, Yingdong Hu, Zehong Lin, and Jun Zhang. Neural representation for wireless radiation field reconstruction: A 3d gaussian splatting approach, 2025. URL <https://arxiv.org/abs/2412.04832>.

[33] Kang Yang, Gaofeng Dong, Sijie Ji, Wan Du, and Mani Srivastava. Scalable 3d gaussian splatting-based rf signal spatial propagation modeling, 2025. URL <https://arxiv.org/abs/2502.01826>.

[34] Hyeongtak Yun, Juntaek Han, Kaiming Shen, and Jeonghun Park. Uplink coordinated pilot design for 1-bit massive mimo in correlated channel. *arXiv preprint arXiv:2502.13429*, 2025.

[35] Xiaopeng Zhao, Zhenlin An, Qingrui Pan, and Lei Yang. Nerf2: Neural radio-frequency radiance fields. In *Proceedings of the 29th Annual International Conference on Mobile Computing and Networking*, ACM MobiCom ’23, page 1–15. ACM, October 2023. doi: 10.1145/3570361.3592527. URL <http://dx.doi.org/10.1145/3570361.3592527>.

A Preliminaries

Signal Propagation

A baseband symbol can be written as $x = Ae^{j\psi}$, where the amplitude A and phase ψ encode the information bits in the complex plane. When a carrier of centre-frequency f propagates a distance d , its amplitude and phase follow the free-space path-loss law ([23])

$$A_{\text{att}}(d) = \frac{c}{4\pi d f}, \quad \Delta\psi(d) = -\frac{2\pi f d}{c} \quad (1)$$

Additional reflections, diffractions, and penetrations inject path-dependent attenuation and phase shifts governed by material properties and incident angles ([23, 11]) as in Figure 5. At the receiver, L distinct propagation paths superimpose, yielding

$$y = \sum_{l=0}^{L-1} A_l A_{\text{att},l} e^{j(\psi + \Delta\psi_l)} \quad (2)$$

where each path l has its own attenuation $A_{\text{att},l}$ and excess phase $\Delta\psi_l$. The *wireless channel* is the complex ratio

$$h = \frac{y}{x} = \sum_{l=0}^{L-1} A_{\text{att},l} e^{j\Delta\psi_l} \quad (3)$$

fully characterizing the distortions imposed by the environment. For an $N_{\text{rx}} \times N_{\text{tx}}$ narrow-band MIMO link, array steering vectors collect the per-path effects into

$$\mathbf{H} = \sum_{l=0}^{L-1} \alpha_l \mathbf{a}_r(\vartheta_l^r) \mathbf{a}_t^H(\vartheta_l^t), \quad \alpha_l = A_{\text{att},l} e^{j\Delta\psi_l} \quad (4)$$

where L is the total number of propagation paths, $\alpha_l = A_{\text{att},l} e^{j\Delta\psi_l}$ is the complex gain of path l , combining its attenuation $A_{\text{att},l}$ and phase shift $\Delta\psi_l$. $\mathbf{a}_t(\vartheta_l^t)$ is the transmit array steering vector at departure angle ϑ_l^t and $\mathbf{a}_r(\vartheta_l^r)$ is the receive array steering vector at arrival angle ϑ_l^r . The 3GPP TR 38.901 clustered delay-line model randomizes $(\alpha_l, \tau_l, \vartheta_l^t, \vartheta_l^r)$ across standardized scenarios from 0.5 GHz to 100 GHz for 5G/6G evaluations. At millimetre-wave bands ($f > 24$ GHz), atmospheric absorption and rain introduce frequency-selective losses that further shorten viable link distances ([22]).

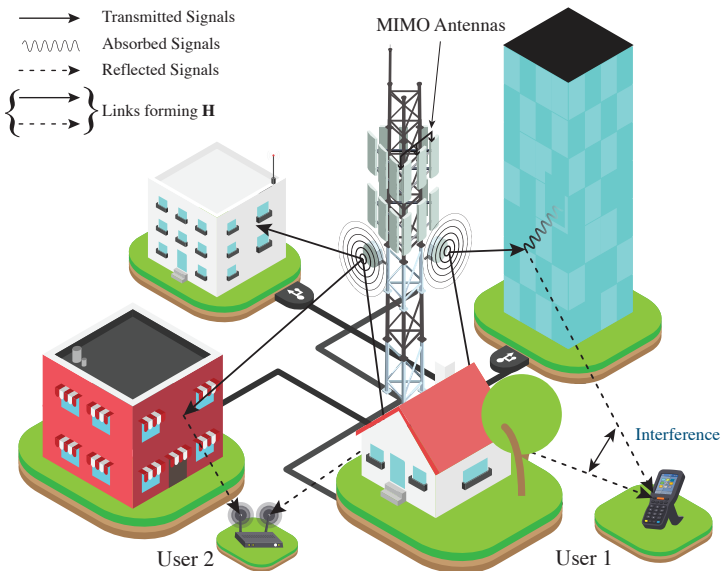


Figure 5: Wireless signal propagation in a multipath environment.

MIMO Channel Estimation

In a MIMO system comprising N_t transmit and N_r receive antennas, the wireless propagation channel is modeled as a complex matrix $\mathbf{H} \in \mathbb{C}^{N_t \times N_r}$, whose accurate estimation is fundamental for coherent demodulation, beamforming, and spatial multiplexing. Let $\mathbf{X} \in \mathbb{C}^{N_t \times T}$ denote the known pilot matrix transmitted over T time slots, and let $\mathbf{Y} \in \mathbb{C}^{N_r \times T}$ be the corresponding received signal matrix. Under a narrowband flat-fading assumption [25], the system model is given by $\mathbf{Y} = \mathbf{H}\mathbf{X} + \mathbf{N}$, where $\mathbf{N} \in \mathbb{C}^{N_r \times T}$ denotes the additive white Gaussian noise (AWGN) with i.i.d. entries $\sim \mathcal{CN}(0, \sigma_n^2)$. The pilot matrix is often chosen to be orthogonal, satisfying $\mathbf{X}\mathbf{X}^H = \rho\mathbf{I}_{N_t}$ for transmit power ρ , which ensures full rank and simplifies the inversion in linear estimators [34].

In scenarios lacking statistical priors, the channel is commonly estimated using the Least Squares (LS) approach by solving $\hat{\mathbf{H}}_{\text{LS}} = \arg \min_{\mathbf{H}} \|\mathbf{Y} - \mathbf{H}\mathbf{X}\|_F^2$, which yields the closed-form solution $\hat{\mathbf{H}}_{\text{LS}} = \mathbf{Y}\mathbf{X}^H(\mathbf{X}\mathbf{X}^H)^{-1}$, provided $\mathbf{X}\mathbf{X}^H$ is invertible. While computationally inexpensive, the LS estimator is agnostic to the stochastic nature of the channel and susceptible to performance degradation under low SNR or pilot contamination.

To incorporate second-order statistics of the channel, a Bayesian framework leads to the Minimum Mean Squared Error (MMSE) estimator. Assuming $\text{vec}(\mathbf{H}) \sim \mathcal{CN}(\mathbf{0}, \mathbf{R}_{hh})$, where $\mathbf{R}_{hh} \in \mathbb{C}^{N_r N_t \times N_r N_t}$ denotes the channel covariance matrix, the MMSE estimator is defined as $\hat{\mathbf{H}}_{\text{MMSE}} = \mathbb{E}[\mathbf{H} | \mathbf{Y}]$. Under jointly Gaussian assumptions and linear observation model, the Wiener filter [29] solution follows as:

$$\hat{\mathbf{H}}_{\text{MMSE}} = \mathbf{R}_{hy} \mathbf{R}_{yy}^{-1} \mathbf{Y} \quad (5)$$

where $\mathbf{R}_{hy} = \mathbb{E}[\mathbf{H}\mathbf{Y}^H] = \mathbf{R}_{hh}\mathbf{X}^H$ and $\mathbf{R}_{yy} = \mathbb{E}[\mathbf{Y}\mathbf{Y}^H] = \mathbf{X}\mathbf{R}_{hh}\mathbf{X}^H + \sigma_n^2\mathbf{I}_T$. Substituting yields the closed-form MMSE estimate:

$$\hat{\mathbf{H}}_{\text{MMSE}} = \mathbf{R}_{hh} \mathbf{X}^H (\mathbf{X}\mathbf{R}_{hh}\mathbf{X}^H + \sigma_n^2\mathbf{I}_T)^{-1} \mathbf{Y} \quad (6)$$

This expression stems from the optimal linear Bayesian estimator or equivalently, from the steady-state solution of the Kalman filter [24]. Intuitively, the MMSE estimator [20] performs a statistically weighted projection of the LS solution, taking into account the prior distribution of \mathbf{H} and the observation noise. For i.i.d. Rayleigh fading [26] with uncorrelated entries, where $\mathbf{R}_{hh} = \sigma_h^2\mathbf{I}$, the expression simplifies to the scalar-weighted LS estimator:

$$\hat{\mathbf{H}}_{\text{MMSE}} = \frac{\sigma_h^2}{\sigma_h^2 + \sigma_n^2/\rho} \hat{\mathbf{H}}_{\text{LS}} \quad (7)$$

which highlights MMSE as a regularized LS estimator and a canonical instance of Wiener filtering [29]. However, its computational complexity—arising from the inversion of a $T \times T$ matrix—and reliance on accurate prior knowledge of \mathbf{R}_{hh} impose practical challenges, especially in massive MIMO scenarios with high-dimensional channels.

3D Gaussian Splatting

3DGS [13] is a technique for representing and rendering scenes using 3D Gaussians as primitive elements, which has gained popularity for its efficiency in graphics. First, we explain the fundamentals of 3DGS in computer graphics. Instead of meshes or voxels, a scene is described by a set of anisotropic 3D Gaussians. The i -th Gaussian is specified by center $\boldsymbol{\mu}_i \in \mathbb{R}^3$, covariance $\boldsymbol{\Sigma}_i \succ 0$, color \mathbf{c}_i and opacity α_i :

$$G_i(\mathbf{x}) = \exp\left[-\frac{1}{2}(\mathbf{x} - \boldsymbol{\mu}_i)^\top \boldsymbol{\Sigma}_i^{-1}(\mathbf{x} - \boldsymbol{\mu}_i)\right]. \quad (8)$$

With $\boldsymbol{\Sigma}_i = \mathbf{R}_i \mathbf{S}_i^2 \mathbf{R}_i^\top$ (rotation \mathbf{R}_i , diagonal scales \mathbf{S}_i) the ellipsoid axes remain positive and differentiable. This is the standard Gaussian equation [7] in \mathbb{R}^3 , which forms an ellipsoidal “bump” centered at $\boldsymbol{\mu}_i$. Intuitively, $\boldsymbol{\Sigma}_i$ (or its inverse $\boldsymbol{\Sigma}_i^{-1}$, the precision matrix) defines the ellipsoid’s axes—if $\boldsymbol{\Sigma}_i = \text{diag}(\sigma_x^2, \sigma_y^2, \sigma_z^2)$ in the Gaussian’s local frame, the point is like an ellipsoid with standard deviations $\sigma_x, \sigma_y, \sigma_z$ along its principal axes. In practice, $\boldsymbol{\Sigma}_i$ is often parameterized by a rotation matrix \mathbf{R}_i and a diagonal scaling matrix \mathbf{S}_i such that $\boldsymbol{\Sigma}_i = \mathbf{R}_i \mathbf{S}_i^2 \mathbf{R}_i^\top$.

A pinhole camera [27] with projection map Π , maps each Gaussian to an image-plane Gaussian. Linearizing Π about μ_i yields the 2×2 covariance of the screen-space ellipse:

$$\Sigma_{i,\text{img}} = \mathbf{J}_i \Sigma_i \mathbf{J}_i^\top, \quad \mathbf{J}_i = \frac{\partial \Pi}{\partial \mathbf{x}} \Big|_{\mathbf{x}=\mu_i}. \quad (9)$$

Thus, rendering reduces to “splats”—elliptical kernels whose size shrinks with depth and elongates with oblique viewing angles and are accumulated in front-to-back order using α -compositing. The size and shape of this ellipse depend on the distance and orientation of the Gaussian relative to the camera.

Spherical Harmonics for View-Dependent Color. In scenes with reflective or view-dependent appearance, the color of a point can change with viewing direction. 3DGS addresses this by associating spherical harmonic (SH) coefficients with each Gaussian to model directional color variation. Directional color is captured by assigning K real SH coefficients $\tau_{i,n}$ per channel to every Gaussian; evaluating the truncated expansion

$$C_i(\mathbf{v}) = \sum_{n=1}^K \tau_{i,n} Y_n(\mathbf{v}), \quad (10)$$

for view direction \mathbf{v} yields its RGB color. Second-order SH ($K = 9$) is usually sufficient; $K = 1$ recovers a constant color.

Alpha Blending and Rendering. To synthesize an image, contributions from projected Gaussians are integrated using 3DGS with overcompositing, akin to front-to-back α -blending in volume rendering. The accumulated pixel color follows:

$$C = \sum_{i=1}^N T_i \alpha_i C_i, \quad T_i = \prod_{j < i} (1 - \alpha_j), \quad (11)$$

where i indexes sorted Gaussians by depth, C_i represents SH-evaluated color, and α_i denotes opacity. A standard per-pixel opacity model is defined as:

$$\tilde{\alpha}_i(u, v) = 1 - \exp[-\Lambda_i G_i(u, v)], \quad (12)$$

with $G_i(u, v)$ as the projected 2D Gaussian density and Λ_i scaling opacity, linking splat blending to NeRF’s volumetric integral. Point-splat blending mathematically mirrors NeRF’s volumetric integration, treating each point akin to a miniature volume element. Sorting of splats is essential, enabled by efficient tile-based rasterization [5] and z-buffer [30] sorting, leveraging Gaussian characteristics for real-time rendering.

B Dataset Generation

To evaluate nGRF effectively, we generate datasets that closely mimic realistic MIMO channels through a physics-based ray tracing approach. We create two complementary dataset types: three detailed indoor environments and one large-scale outdoor scenario. For both scenarios, we begin by importing 3D models (STL files) of the environments and extracting their geometric properties (vertices and faces). Indoor environments feature fine details of room layouts, furniture, and structural elements, while outdoor environments represent buildings, terrain variations, and urban features with corresponding complexity. These environmental models provide the necessary geometric foundation for accurate ray tracing and propagation simulation.

The propagation itself is simulated using MATLAB’s RayTracing object. In indoor scenarios, we position a URA as the transmitter, while receivers (functioning as “data samples”) are randomly distributed throughout the space. The outdoor scenario follows a similar methodology but encompasses extensive propagation ranges and environmental complexity.

Each transmitter-receiver pair generates multiple propagation paths computed through the ray tracing simulator. Our channel modeling is based on the complex interactions between electromagnetic waves and the environment. For each ray path, we first compute the free-space path loss (FSPL) according to:

$$\text{FSPL (dB)} = 20 \log_{10}(d) + 20 \log_{10}(f) + 20 \log_{10} \left(\frac{4\pi}{c} \right), \quad (13)$$

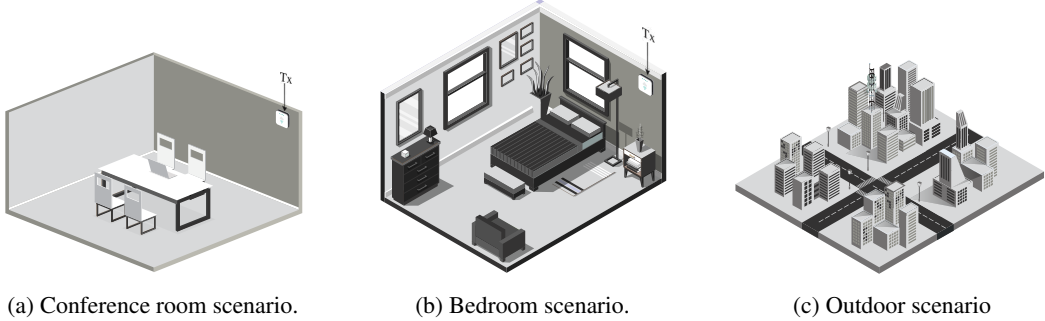


Figure 6: 3D environment models for simulation demonstrating different outdoor and indoor environments.

where d is the propagation distance in meters, f is the carrier frequency in Hz, and c is the speed of light. This equation models the power attenuation of a signal as it travels through free space without obstacles or reflections. The phase shift, on the other hand, is calculated based on the propagation distance as $\phi = -2\pi f \tau$, where τ is the propagation delay and d is the total path length.

For more complex interactions, such as reflections and diffractions, we make use of the uniform theory of diffraction (UTD) and the Fresnel equations to calculate additional losses. When a ray reflects off a surface, the reflection coefficient is computed based on the material properties, incidence angle, and signal polarization. For each reflection point, the reflection coefficient is calculated as:

$$\Gamma_p = \frac{\sin \theta_i - \sqrt{\varepsilon_r - \cos^2 \theta_i}}{\sin \theta_i + \sqrt{\varepsilon_r - \cos^2 \theta_i}}, \quad (14)$$

and

$$\Gamma_s = \frac{\varepsilon_r \sin \theta_i - \sqrt{\varepsilon_r - \cos^2 \theta_i}}{\varepsilon_r \sin \theta_i + \sqrt{\varepsilon_r - \cos^2 \theta_i}}, \quad (15)$$

where Γ_p and Γ_s represent the reflection coefficients for parallel and perpendicular polarization components, θ_i is the incidence angle, and ε_r is the complex relative permittivity of the reflecting material. The permittivity depends on the type of material, such as concrete, glass, or wood (information which is embedded into the STL), and the signal frequency.

To construct the MIMO channel matrix \mathbf{H} , we integrate the contributions from all significant propagation paths between the transmitter and receiver. For a system with N_t transmit antennas and N_r receive antennas, the channel matrix $\mathbf{H} \in \mathbb{C}^{N_t \times N_r}$ is computed by processing the ray tracing results.

For multi-antenna systems, we incorporate array geometry through steering vectors. For the transmitting array with URA configuration, the steering vector \mathbf{a}_T is computed as:

$$\mathbf{a}_T(f, [\alpha_T; \beta_T]) = \exp \left(j \frac{2\pi f}{c} \mathbf{d}_T \cdot [\cos \alpha_T \cos \beta_T, \sin \alpha_T \cos \beta_T, \sin \beta_T]^T \right) \quad (16)$$

where \mathbf{d}_T represents the positions of the transmit array elements relative to the reference element. The steering vector \mathbf{a}_R for a receiving array with a ULA configuration can be computed in a similar fashion. The channel matrix for a single ray path is given by:

$$\mathbf{H}_l = a_l e^{j\phi_l} \mathbf{a}_R \mathbf{a}_T^H, \quad (17)$$

where $(\cdot)^H$ denotes the Hermitian transpose. The overall channel matrix is the sum of contributions from all ray paths:

$$\mathbf{H} = \sum_{l=0}^{L-1} \mathbf{H}_l = \sum_{l=0}^{L-1} a_l e^{j\phi_l} \mathbf{a}_R \mathbf{a}_T^H \quad (18)$$

For SISO configurations, where both transmitter and receiver have a single antenna, the channel simplifies to a complex scalar value computed as the sum of all multipath components:

$$h = \sum_{l=0}^{L-1} a_l e^{j\phi_l}, \quad (19)$$

Algorithm 2: Build Rotation Matrix from Quaternion

Require : Unit quaternion $\mathbf{q} = [q_w, q_x, q_y, q_z]^\top$
Ensure : Rotation matrix $\mathbf{R} \in SO(3)$

- 1 $\mathbf{R} \leftarrow \mathbf{0} \in \mathbb{R}^{3 \times 3}$
 $\quad //$ Compute squared terms
- 2 $q_x^2 \leftarrow q_x \cdot q_x$
- 3 $q_y^2 \leftarrow q_y \cdot q_y$
- 4 $q_z^2 \leftarrow q_z \cdot q_z$
 $\quad //$ Compute product terms
- 5 $q_{xy} \leftarrow q_x \cdot q_y$
- 6 $q_{xz} \leftarrow q_x \cdot q_z$
- 7 $q_{yz} \leftarrow q_y \cdot q_z$
- 8 $q_{wx} \leftarrow q_w \cdot q_x$
- 9 $q_{wy} \leftarrow q_w \cdot q_y$
- 10 $q_{wz} \leftarrow q_w \cdot q_z$
- 11 $\mathbf{R}_{00} \leftarrow 1 - 2(q_y^2 + q_z^2)$
- 12 $\mathbf{R}_{01} \leftarrow 2(q_{xy} - q_{wz})$
- 13 $\mathbf{R}_{02} \leftarrow 2(q_{xz} + q_{wy})$
- 14 $\mathbf{R}_{10} \leftarrow 2(q_{xy} + q_{wz})$
- 15 $\mathbf{R}_{11} \leftarrow 1 - 2(q_x^2 + q_z^2)$
- 16 $\mathbf{R}_{12} \leftarrow 2(q_{yz} - q_{wx})$
- 17 $\mathbf{R}_{20} \leftarrow 2(q_{xz} - q_{wy})$
- 18 $\mathbf{R}_{21} \leftarrow 2(q_{yz} + q_{wx})$
- 19 $\mathbf{R}_{22} \leftarrow 1 - 2(q_x^2 + q_y^2)$
- 20 **Return** \mathbf{R}

where a_l is the amplitude attenuation and ϕ_l is the phase shift for the l -th path. This scalar complex channel represents the aggregate effect of all propagation paths between the single transmit and receive antennas.

C nGRF: Implementation Details

Forward Pass

Gaussian Parameterization. In nGRF, each volumetric Gaussian primitive G_i is parameterized by a center position $\mu_i \in \mathbb{R}^3$, a rotation $\mathbf{q}_i \in \mathbb{R}^4$ (represented as a unit quaternion), and a scaling vector $\mathbf{s}_i \in \mathbb{R}^3$. The rotation and scaling together define the shape of the Gaussian through a covariance matrix Σ_i . Unlike previous approaches that use naive projections, nGRF directly models radio wave phenomena via 3D electromagnetic field aggregation, where Gaussians act as localized radio modulators.

The position parameter μ_i represents the Gaussian center in 3D space. The rotation parameter $\mathbf{q}_i = [q_w, q_x, q_y, q_z]^\top$ encodes the orientation of the Gaussian and is constrained to be a unit quaternion ($\|\mathbf{q}_i\|_2 = 1$). The scaling parameters $\mathbf{s}_i = [s_1, s_2, s_3]^\top$ represent the extent of the Gaussian along its principal axes. To ensure the Gaussian has positive scaling along all axes, we parameterize \mathbf{s}_i as exponentials of unconstrained parameters \mathbf{s}'_i :

$$\mathbf{s}_i = \exp(\mathbf{s}'_i) \quad (20)$$

Covariance Matrix Construction. The covariance matrix Σ_i determines the shape and orientation of each Gaussian. It is constructed from the rotation matrix \mathbf{R}_i (derived from the quaternion \mathbf{q}_i) and the scale matrix $\mathbf{S}_i = \text{diag}(\mathbf{s}_i)$:

$$\Sigma_i = \mathbf{R}_i \mathbf{S}_i^2 \mathbf{R}_i^\top \quad (21)$$

The rotation matrix $\mathbf{R}_i \in \mathbb{R}^{3 \times 3}$ is computed from the quaternion using Algorithm 2, which is the implementation of Rodrigues' rotation formula. The quaternion \mathbf{q}_i is normalized to ensure it

Algorithm 3: Build Inverse Covariance Matrix

Require : Rotation matrix $\mathbf{R} \in \mathbb{R}^{3 \times 3}$, scaling factors $\mathbf{s} \in \mathbb{R}^3$, small value ϵ
Ensure : Inverse covariance matrix $\Sigma^{-1} \in \mathbb{R}^{3 \times 3}$

```

// Clamp scaling to prevent division by zero
1  $\mathbf{s}_{\text{clamped}} \leftarrow \max(\mathbf{s}, \epsilon)$ 
// Compute inverse squared scaling
2  $\mathbf{s}_{\text{inv_sq}} \leftarrow 1.0 / (\mathbf{s}_{\text{clamped}} \cdot \mathbf{s}_{\text{clamped}})$ 
// Create diagonal matrix from inverse squared scaling
3  $\mathbf{S}_{\text{inv_sq}} \leftarrow \text{diag\_embed}(\mathbf{s}_{\text{inv_sq}})$ 
// Apply rotation to inverse scaling
4  $\Sigma^{-1} \leftarrow \mathbf{R} \cdot \mathbf{S}_{\text{inv_sq}} \cdot \mathbf{R}^\top$ 
5 Return  $\Sigma^{-1}$ 

```

represents a valid rotation. The rotation matrix is constructed as follows:

$$\mathbf{R}_i = \begin{bmatrix} 1 - 2(q_{i,y}^2 + q_{i,z}^2) & 2(q_{i,x}q_{i,y} - q_{i,w}q_{i,z}) & 2(q_{i,x}q_{i,z} + q_{i,w}q_{i,y}) \\ 2(q_{i,x}q_{i,y} + q_{i,w}q_{i,z}) & 1 - 2(q_{i,x}^2 + q_{i,z}^2) & 2(q_{i,y}q_{i,z} - q_{i,w}q_{i,x}) \\ 2(q_{i,x}q_{i,z} - q_{i,w}q_{i,y}) & 2(q_{i,y}q_{i,z} + q_{i,w}q_{i,x}) & 1 - 2(q_{i,x}^2 + q_{i,y}^2) \end{bmatrix}, \quad (22)$$

This conversion ensures that \mathbf{R}_i is an orthogonal matrix belonging to $SO(3)$, the special orthogonal group of 3D rotations.

For channel estimation, we often need the inverse covariance matrix Σ_i^{-1} to compute Mahalanobis distances. Rather than explicitly inverting Σ_i , we construct the inverse covariance matrix directly using Algorithm 3.

Neural Architecture. Each Gaussian is associated with latent features and a base activation that are generated by neural networks. These attributes determine the electromagnetic behavior of the Gaussian primitive. As described in the main text, we use two neural networks to compute the latent features and channel contributions:

- *Attribute Network*: This network takes as input the Gaussian center μ_i and the transmitter position \mathbf{p}_{tx} , and outputs a latent feature vector $\mathbf{z}_i \in \mathbb{R}^d$ and a base activation logit $\alpha'_i \in \mathbb{R}$.
- *Contribution Decoder Network*: This network takes the latent features \mathbf{z}_i and outputs complex channel contributions $\mathbf{C}_i \in \mathbb{C}^{N_t \times N_r}$.

The network architectures consist of multi-layer perceptrons (MLPs) with position encoding to better capture high-frequency spatial variations.

$$\gamma_L(\mathbf{x}) = [\mathbf{x}, \sin(2^0 \pi \mathbf{x}), \cos(2^0 \pi \mathbf{x}), \dots, \sin(2^{L-1} \pi \mathbf{x}), \cos(2^{L-1} \pi \mathbf{x})], \quad (23)$$

$$[\mathbf{z}_i, \alpha'_i] = f_{\text{attr}}(\gamma_L(\mu_i), \gamma_L(\mathbf{p}_{\text{tx}})), \quad (24)$$

$$\mathbf{C}_i = f_{\text{dec}}(\mathbf{z}_i) \quad (25)$$

The base activation α_i is computed by applying a sigmoid function to the logit α'_i :

$$\alpha_i = \sigma(\alpha'_i) = \frac{1}{1 + \exp(-\alpha'_i)} \quad (26)$$

Spatial Weight Computation. For a receiver position \mathbf{p}_{rx} , we compute the *spatial weight* of each Gaussian to determine its contribution to the received signal. This weight is based on the Mahalanobis distance between the receiver and the Gaussian center:

$$w_i(\mathbf{p}_{\text{rx}}) = \alpha_i \exp\left(-\frac{1}{2}(\mathbf{p}_{\text{rx}} - \mu_i)^\top \Sigma_i^{-1}(\mathbf{p}_{\text{rx}} - \mu_i)\right) \quad (27)$$

The exponential term represents the probability density function of the Gaussian evaluated at the receiver position, modulating the base activation α_i . This formulation captures the spatial decay of electromagnetic influence with distance, accounting for the anisotropic shape of the Gaussian.

Channel Matrix Rendering. The final MIMO channel matrix $\mathbf{H}(\mathbf{p}_{\text{rx}}, \mathbf{p}_{\text{tx}}) \in \mathbb{C}^{N_t \times N_r}$ is computed as a weighted sum of complex contributions from all Gaussian primitives:

$$\mathbf{H}(\mathbf{p}_{\text{rx}}, \mathbf{p}_{\text{tx}}) = \sum_{i=1}^N w_i(\mathbf{p}_{\text{rx}}, \boldsymbol{\mu}_i, \boldsymbol{\Sigma}_i) \cdot \mathbf{C}_i \quad (28)$$

Unlike ray-tracing or volumetric approaches, this direct summation makes the computation efficient with complexity $\mathcal{O}(N N_t N_r)$, where N is the number of Gaussian primitives. The entire process is summarized in Algorithm 1.

Backward Pass

The backward pass of nGRF computes gradients with respect to all trainable parameters, enabling end-to-end optimization. We derive the gradients analytically to ensure computational efficiency and numerical stability.

Channel Matrix Gradient. Given a loss function \mathcal{L} and its gradient with respect to the predicted channel matrix $\frac{\partial \mathcal{L}}{\partial \mathbf{H}}$, we compute gradients for each component of the forward pass.

For the weighted complex sum, the gradients with respect to weights w_i and contributions \mathbf{C}_i are:

$$\frac{\partial \mathcal{L}}{\partial w_i} = \text{Re} \left(\sum_{j,k} \frac{\partial \mathcal{L}}{\partial \mathbf{H}_{j,k}} \cdot \mathbf{C}_{i,j,k}^* \right), \quad (29)$$

$$\frac{\partial \mathcal{L}}{\partial \mathbf{C}_i} = \sum_b w_{b,i} \cdot \frac{\partial \mathcal{L}}{\partial \mathbf{H}_b} \quad (30)$$

where \mathbf{C}_i^* denotes the complex conjugate of \mathbf{C}_i .

Spatial Weighting Gradients. For the spatial weight computation, we backpropagate through the Mahalanobis distance calculation. Let $m_i^2 = (\mathbf{p}_{\text{rx}} - \boldsymbol{\mu}_i)^\top \boldsymbol{\Sigma}_i^{-1} (\mathbf{p}_{\text{rx}} - \boldsymbol{\mu}_i)$ be the squared Mahalanobis distance. The gradient with respect to various components is:

$$\frac{\partial \mathcal{L}}{\partial \alpha_i} = \frac{\partial \mathcal{L}}{\partial w_i} \cdot \exp \left(-\frac{1}{2} m_i^2 \right), \quad (31)$$

$$\frac{\partial \mathcal{L}}{\partial m_i^2} = \frac{\partial \mathcal{L}}{\partial w_i} \cdot w_i \cdot \left(-\frac{1}{2} \right), \quad (32)$$

$$\frac{\partial \mathcal{L}}{\partial (\mathbf{p}_{\text{rx}} - \boldsymbol{\mu}_i)} = \frac{\partial \mathcal{L}}{\partial m_i^2} \cdot 2\boldsymbol{\Sigma}_i^{-1}(\mathbf{p}_{\text{rx}} - \boldsymbol{\mu}_i), \quad (33)$$

$$\frac{\partial \mathcal{L}}{\partial \boldsymbol{\Sigma}_i^{-1}} = \frac{\partial \mathcal{L}}{\partial m_i^2} \cdot (\mathbf{p}_{\text{rx}} - \boldsymbol{\mu}_i)(\mathbf{p}_{\text{rx}} - \boldsymbol{\mu}_i)^\top \quad (34)$$

Rotation and Scaling Parameter Adjoints. For the quaternion \mathbf{q}_i and scaling parameters \mathbf{s}_i , we need to backpropagate through the covariance matrix construction:

$$\frac{\partial \mathcal{L}}{\partial \mathbf{q}_i} = \frac{\partial \mathcal{L}}{\partial \mathbf{R}_i} \cdot \frac{\partial \mathbf{R}_i}{\partial \mathbf{q}_i}, \quad (35)$$

$$\frac{\partial \mathcal{L}}{\partial \mathbf{s}_i} = \frac{\partial \mathcal{L}}{\partial \boldsymbol{\Sigma}_i^{-1}} \cdot \frac{\partial \boldsymbol{\Sigma}_i^{-1}}{\partial \mathbf{s}_i} \quad (36)$$

The gradient of the rotation matrix with respect to quaternion parameters involves a series of chain rule applications through the quaternion-to-rotation conversion. Similarly, the gradient with respect to scaling parameters flows through the inverse covariance matrix construction.

Neural Attributes. The gradients with respect to the attribute network and decoder network parameters follow standard backpropagation for neural networks:

$$\frac{\partial \mathcal{L}}{\partial \theta_{\text{attr}}} = \frac{\partial \mathcal{L}}{\partial \mathbf{z}_i} \cdot \frac{\partial \mathbf{z}_i}{\partial \theta_{\text{attr}}} + \frac{\partial \mathcal{L}}{\partial \alpha'_i} \cdot \frac{\partial \alpha'_i}{\partial \theta_{\text{attr}}}, \quad (37)$$

$$\frac{\partial \mathcal{L}}{\partial \theta_{\text{dec}}} = \frac{\partial \mathcal{L}}{\partial \mathbf{C}_i} \cdot \frac{\partial \mathbf{C}_i}{\partial \theta_{\text{dec}}} \quad (38)$$

where θ_{attr} and θ_{dec} represent the trainable parameters of the attribute and decoder networks, respectively.

Implementation Tricks

CUDA Implementation. We implemented custom CUDA kernels for the most computationally intensive operations in nGRF. The forward and backward passes of the core operations—quaternion normalization, rotation matrix construction, spatial weight computation, and complex weighted summation—are optimized in CUDA for parallel execution across Gaussians and are the core reason why our implementation can infer the channel matrix in 1.1 ms.

Moreover, to address the variable computational load across different Gaussians (due to their spatial distribution relative to receivers), a dynamic work distribution scheme is implemented in CUDA; effectively balancing the workload across streaming multiprocessors and reducing thread divergence within warps.

Fused Ops. Multiple mathematical operations are fused into single kernels to minimize memory transfers and kernel launches. For example, the computation of spatial weights combines the Mahalanobis distance calculation, exponentiation, and activation scaling in a single kernel. Similarly, the rotation matrix construction and inverse covariance computation are fused to eliminate intermediate storage.

Numerical Stability. To ensure no gradient explodes or vanishes, common numerical stability techniques are used:

1. When computing the Mahalanobis distance, we clamp the result to a maximum value (typically 50.0) before exponentiation to prevent overflow.
2. In the inverse covariance computation, we add a small positive value to the diagonal elements to ensure positive definiteness.
3. For quaternion normalization, we use a numerically stable approach with epsilon-clamping to avoid division by zero.

Batch Processing. Instead of processing each receiver position independently, unlike in previous works, we process multiple receiver positions in a batch. For each batch, we compute the attribute network outputs once and reuse them across all receiver positions. This relies on the fact that the attribute network outputs depend only on the Gaussian centers and the transmitter position, not on receiver positions.

Parameter Grouping. During optimization, we organize parameters into groups with different learning rates and update schedules. Position parameters (μ_i) use an exponentially decaying learning rate schedule, while rotation, scaling, and neural network parameters use constant learning rates. This grouping allows for fine-grained control over the optimization process and improves training stability.

D [Case Study] Gaussian Scatterer Centric Radio Field Construction

Motivation

Classical geometry-based stochastic models (GBSMs) [4] represent multipath components as point scatterers, but lose spatial smoothness and differentiability that modern neural renderers exploit. Instead, we embed every physical scatterer inside an anisotropic 3-D *Gaussian ellipsoid* whose density encodes its geometric extent and scattering transfer function. This *scatterer-Gaussian* abstraction preserves the first-order physics Fresnel zone support, far-field phase curvature, and path-loss exponent, while admitting closed-form convolution with the free-space Green’s function [8]. The Gaussian basis remains differentiable, enabling gradient back-propagation through the radio channel. We optimize our approach on CUDA kernels to make it **350**× faster than the equivalent PyTorch implementation.

Forward Pass

Gaussian Scatterer Parameterization. In this *case study 1*, we treat each multipath scatterer as a trivariate normal $\mathcal{N}(\mu, \Sigma)$; the mean $\mu \in \mathbb{R}^3$ denotes the centroid of energy, while the covariance $\Sigma \in \mathbb{R}^{3 \times 3}$ controls its anisotropic spread. The covariance is generated from two sets of learnable parameters: a unit quaternion $\mathbf{q} = [w, x, y, z]^\top$ with w, x, y and z as the quaternion components, encoding spatial orientation; a positive scaling triple $\alpha_s = [\alpha_{s_1}, \alpha_{s_2}, \alpha_{s_3}]^\top$, with $\alpha_{s_1}, \alpha_{s_2}$, and α_{s_3} are the scaling factors of major, intermediate and minor principal axes respectively.

The forward computation proceeds in four differentiable steps. The quaternion is mapped to an orthogonal matrix $R(\mathbf{q}) \in \text{SO}(3)$ via the classic homomorphism [17]:

$$R(\mathbf{q}) = \begin{bmatrix} 1 - 2(y^2 + z^2) & 2(xy - wz) & 2(xz + wy) \\ 2(xy + wz) & 1 - 2(x^2 + z^2) & 2(yz - wx) \\ 2(xz - wy) & 2(yz + wx) & 1 - 2(x^2 + y^2) \end{bmatrix}. \quad (39)$$

We form an axis-aligned scaling matrix:

$$S = \text{diag}(\alpha_{s_1}, \alpha_{s_2}, \alpha_{s_3}), \quad (40)$$

where each $\alpha_{s_k} > 0$ is produced by an MLP with softplus activation to ensure positivity. Combining orientation and scale gives the matrix:

$$RS = R(\mathbf{q}) S, \quad (41)$$

which aligns the scatterer's principal axes with the spatial frame captured by \mathbf{q} . The covariance of the Gaussian scatterer is the symmetric positive-definite matrix

$$\Sigma = RS (RS)^\top. \quad (42)$$

Because Σ is constructed directly from RS , Cholesky factorization is not needed during training or inference. Equations (39)-(42) are fully vectorized and run in < 0.01 ms per scatterer on an NVIDIA RTX 5090, introducing negligible overhead relative to volumetric rendering.

Angular Projection to Channel Grid. For each Gaussian scatterer k and each receiver element j (with center position \mathbf{r}_j), we project the scatterer's centroid \mathbf{p}_k onto the discrete (u, v) -grid of the channel matrix $\mathbf{H} \in \mathbb{C}^{N_t \times N_r}$. Where N_t is the total number of **transmit** antenna elements, and N_r is the total number of **receive** antenna elements. The complete, vectorized mapping is organized into four logical steps as follows. *We first compute the Cartesian offset \mathbf{d}_{kj} from receiver to scatterer and its Euclidean norm r_{kj} . These quantities localize the path in 3D space and provide the geometric baseline for subsequent angular calculations.*

$$\mathbf{d}_{kj} = \mathbf{p}_k - \mathbf{r}_j, \quad r_{kj} = \|\mathbf{d}_{kj}\|_2. \quad (43)$$

The offset vector is re-expressed in spherical coordinates. Longitude Ω_{lon} captures azimuth, while latitude Ω_{lat} captures elevation, together defining the scatterer's direction of arrival at the receiver.

$$\Omega_{\text{lon}} = \text{atan2}(d_{kj,y}, d_{kj,x}), \quad \Omega_{\text{lat}} = \arcsin(d_{kj,z}/r_{kj}). \quad (44)$$

Angles are scaled to the unit square $[-1, +1]^2$ to obtain dimensionless coordinates (s_x, s_y) . This normalization decouples the projection from absolute angular ranges and simplifies indexing.

$$s_x = \frac{\Omega_{\text{lon}}}{\pi}, \quad s_y = \frac{2\Omega_{\text{lat}}}{\pi}. \quad (45)$$

Finally, the unit-square coordinates are affinely mapped onto the discrete transmit-receive grid. The half-pixel shift (+0.5) centres each index, ensuring a symmetric sampling of the angular domain.

$$u_{ki} = (s_x + \frac{1}{2})(N_t - 1) + 0.5, \quad (46)$$

$$v_{kj} = (s_y + \frac{1}{2})(N_r - 1) + 0.5, \quad (47)$$

Where u_{ki} and v_{kj} are the fractional grid index along the transmit and receive axes. Equations (43)-(47) merge the multiple coordinate transform kernels of the original implementation into a single, fully vectorized operation, reducing memory traffic and kernel launches. The mapping ensures

that the angular support of each Gaussian is accurately rasterized onto the (u, v) domain used by subsequent antenna-array processing.

Propagation via Jacobian. To propagate spatial-domain uncertainties through the projection, we require the Jacobian $J_{kj} \in \mathbb{R}^{2 \times 3}$, which linearly approximates the mapping $\mathbf{p}_k \mapsto (u_{ki}, v_{kj})$ around each receiver-scatterer pair (k, j) .

The 2×3 Jacobian gathers the first-order derivatives of the channel-grid coordinates with respect to Cartesian displacements, giving a complete linear sensitivity map from 3-D space to the (u, v) domain as:

$$J_{kj} = \begin{bmatrix} \frac{\partial u_{ki}}{\partial x} & \frac{\partial u_{ki}}{\partial y} & \frac{\partial u_{ki}}{\partial z} \\ \frac{\partial v_{kj}}{\partial x} & \frac{\partial v_{kj}}{\partial y} & \frac{\partial v_{kj}}{\partial z} \end{bmatrix}, \quad (48)$$

where $(x, y, z)^\top = \mathbf{d}_{kj}$ is the displacement vector of Eq. (43).

Expressing the derivatives in closed form reveals how azimuth (row 1) and elevation (row 2) scale with array size and geometry, with singular behaviour gracefully handled by the ρ and γ terms. Let $\rho^2 = x^2 + y^2$ and $\gamma^2 = 1 - (z/r_{kj})^2$; then

$$J_{kj} = \begin{bmatrix} -\frac{N_t - 1}{2\pi} \frac{y}{\rho^2} & \frac{N_t - 1}{2\pi} \frac{x}{\rho^2} & 0 \\ \frac{N_r - 1}{\pi} \frac{z x}{r_{kj} \gamma \rho^2} & \frac{N_r - 1}{\pi} \frac{z y}{r_{kj} \gamma \rho^2} & \frac{N_r - 1}{\pi} \frac{1}{r_{kj} \gamma} \end{bmatrix}. \quad (49)$$

The first row captures azimuthal sensitivity: infinitesimal shifts orthogonal to the displacement vector rotate the longitude and hence u_{ki} . The second row quantifies how both horizontal and vertical perturbations affect elevation, modulating v_{kj} with a $1/\gamma$ factor that inflates derivatives near the horizon. Equation (49) is evaluated in closed form with no branching, allowing the entire Jacobian tensor $\{J_{kj}\}_{k,j}$ to be fused into a single GPU kernel for efficient back-propagation.

2D Covariance Splatting. The spatial uncertainty of each scatterer in the (u, v) plane is obtained by linearly propagating the full 3-D covariance through the Jacobian of Eq. (48):

$$\Sigma_{k,j}^{2D} = J_{kj} \Sigma_k^{3D} J_{kj}^\top. \quad (50)$$

To guarantee numerical stability during subsequent inverse or log-det operations, we add a vanishing jitter $\epsilon \mathbf{I}_2$ with $\epsilon = 10^{-6}$ to the diagonal of $\Sigma_{k,j}^{2D}$, thereby preserving positive definiteness without altering the statistical geometry.

Spatial Influence Kernel Evaluation. *Each scatterer contributes to a channel-matrix element through an anisotropic Gaussian kernel in the (u, v) plane; the kernel value falls off with the Mahalanobis distance [18] between the scatterer's projected location and the antenna's grid position.*

$$\sigma_{kij} = \exp\left(-\frac{1}{2} (\mathbf{u}\mathbf{v}_k - \mathbf{a}_{ij})^\top (\Sigma_{k,j}^{2D})^{-1} (\mathbf{u}\mathbf{v}_k - \mathbf{a}_{ij})\right), \quad (51)$$

where

$$\mathbf{u}\mathbf{v}_k = \begin{bmatrix} u_{ki} \\ v_{kj} \end{bmatrix}, \quad \mathbf{a}_{ij} = \begin{bmatrix} i + \frac{1}{2} \\ j + \frac{1}{2} \end{bmatrix}, \quad (\Sigma_{k,j}^{2D})^{-1} \text{ is the precision of Eq. (50).}$$

The resulting weight $\sigma_{kij} \in (0, 1]$ modulates the complex amplitude that scatterer k imparts to antenna element (i, j) , ensuring spatially coherent aggregation across the channel matrix.

Exact Path Geometry Computation. For each scatterer k we evaluate the exact transmitter-scatterer-receiver geometry needed for physical-channel synthesis. *We form the directed displacement vectors from the transmitter (TX) to the Gaussian centroid and from that centroid to the receiver (RX).*

$$\mathbf{v}_{\text{tx} \rightarrow \text{gauss}} = \mathbf{p}_k - \mathbf{p}_{\text{tx}}, \quad (52)$$

$$\mathbf{v}_{\text{gauss} \rightarrow \text{rx}} = \mathbf{p}_{\text{rx}} - \mathbf{p}_k. \quad (53)$$

The Euclidean norms of these vectors give the precise geometric delays for the two hops.

$$d_{\text{tx}} = \|\mathbf{v}_{\text{tx} \rightarrow \text{gauss}}\|_2, \quad (54)$$

$$d_{\text{rx}} = \|\mathbf{v}_{\text{gauss} \rightarrow \text{rx}}\|_2. \quad (55)$$

Azimuth ϕ is recovered via atan2, while elevation θ follows from the arcsin of the vertical component; Together they specify the full 3-D departure and arrival directions.

$$\phi_{\text{AOD}} = \text{atan2}(v_{\text{tx} \rightarrow \text{gauss},y}, v_{\text{tx} \rightarrow \text{gauss},x}), \quad (56)$$

$$\theta_{\text{AOD}} = \arcsin\left(\frac{v_{\text{tx} \rightarrow \text{gauss},z}}{d_{\text{tx}}}\right), \quad (57)$$

$$\phi_{\text{AOA}} = \text{atan2}(v_{\text{gauss} \rightarrow \text{rx},y}, v_{\text{gauss} \rightarrow \text{rx},x}), \quad (58)$$

$$\theta_{\text{AOA}} = \arcsin\left(\frac{v_{\text{gauss} \rightarrow \text{rx},z}}{d_{\text{rx}}}\right), \quad (59)$$

Where, ϕ_{AOD} is the departure azimuth, θ_{AOD} is the departure elevation, ϕ_{AOA} is the arrival azimuth, and θ_{AOA} is the arrival elevation.

Array Steering Vector Construction. The steering vector encodes the phase offsets across array elements for a plane wave arriving from elevation θ and azimuth ϕ . Its analytic form depends on the array topology. For an $M \times N$ planar grid with element coordinates (x_m, y_n) , the 2-D steering vector factorizes into separable phase ramps along the x - and y -axes.

$$\mathbf{a}_{\text{URA}}(\theta, \phi) = \exp\left(-j k \cos \theta [x_m \cos \phi + y_n \sin \phi]\right), \quad (60)$$

where $k = 2\pi/\lambda$ is the wavenumber and $j = \sqrt{-1}$ follows RF phasor convention. For one-dimensional line of elements at positions x_i , the steering vector reduces to a single exponential that varies only along the array axis.

$$\mathbf{a}_{\text{ULA}}(\theta, \phi) = \exp\left(-j k x_i \cos \theta \cos \phi\right). \quad (61)$$

Equations (60) and (61) supply the phase references required for beamforming and are used in the channel-estimation kernels that follow.

Scattered Path Synthesis. A single reflection via scatterer k produces a rank-one update to the narrowband MIMO channel. The update is constructed from the geometric path loss, the complex scattering coefficient, and the outer product of TX/RX steering vectors. Free-space loss decays with distance d_{path} , while the propagation phase accumulates proportionally to the same distance.

$$\alpha_{\text{amp}} = \frac{\lambda}{4\pi d_{\text{path}}}, \quad \alpha_{\text{phase}} = -\frac{2\pi d_{\text{path}}}{\lambda}, \quad (62)$$

$$\alpha_{\text{real}} = \alpha_{\text{amp}} \cos(\alpha_{\text{phase}}), \quad \alpha_{\text{imag}} = \alpha_{\text{amp}} \sin(\alpha_{\text{phase}}). \quad (63)$$

The scatterer's intrinsic complex gain $\gamma = \gamma_{\text{real}} + j\gamma_{\text{imag}}$ modulates the propagation term, yielding the effective path coefficient $\beta = \beta_{\text{real}} + j\beta_{\text{imag}}$.

$$\beta_{\text{real}} = \gamma_{\text{real}} \alpha_{\text{real}} - \gamma_{\text{imag}} \alpha_{\text{imag}}, \quad (64)$$

$$\beta_{\text{imag}} = \gamma_{\text{real}} \alpha_{\text{imag}} + \gamma_{\text{imag}} \alpha_{\text{real}}. \quad (65)$$

Let \mathbf{sv}_{tx} and \mathbf{sv}_{rx} denote the transmit and receive steering vectors, each decomposed into real and imaginary parts. Their Kronecker outer product yields the rank-one spatial signature of the path.

$$P_{\text{real}} = \mathbf{sv}_{\text{rx},\text{real}} \otimes \mathbf{sv}_{\text{tx},\text{real}} + \mathbf{sv}_{\text{rx},\text{imag}} \otimes \mathbf{sv}_{\text{tx},\text{imag}}, \quad (66)$$

$$P_{\text{imag}} = \mathbf{sv}_{\text{rx},\text{imag}} \otimes \mathbf{sv}_{\text{tx},\text{real}} - \mathbf{sv}_{\text{rx},\text{real}} \otimes \mathbf{sv}_{\text{tx},\text{imag}}. \quad (67)$$

Combining the effective coefficient with the steering product gives the scattered contribution to the complex channel matrix $\mathbf{H} = \mathbf{H}_{\text{real}} + j\mathbf{H}_{\text{imag}}$.

$$\mathbf{H}_{\text{real}} = \beta_{\text{real}} P_{\text{real}} - \beta_{\text{imag}} P_{\text{imag}}, \quad (68)$$

$$\mathbf{H}_{\text{imag}} = \beta_{\text{real}} P_{\text{imag}} + \beta_{\text{imag}} P_{\text{real}}. \quad (69)$$

The pair $(\mathbf{H}_{\text{real}}, \mathbf{H}_{\text{imag}})$ forms a single-bounce rank-one update; summing over all scatterers recovers the full narrowband MIMO channel response.

Line-of-Sight Path Synthesis. The line-of-sight (LOS) signal skips the Gaussian-scatterer layer and is therefore treated as a fixed, non-differentiable update to the MIMO channel. Its amplitude,

phase, and spatial signature follow directly from free-space propagation and array geometry. *The displacement vector and its norm provide distance and pointing direction for the LOS ray.*

$$\mathbf{v}_{\text{tx} \rightarrow \text{rx}} = \mathbf{p}_{\text{rx}} - \mathbf{p}_{\text{tx}}, \quad d_{\text{tx} \rightarrow \text{rx}} = \|\mathbf{v}_{\text{tx} \rightarrow \text{rx}}\|_2. \quad (70)$$

Amplitude decays with $1/d$ while phase rotates by $2\pi d/\lambda$, yielding the real and imaginary parts of the complex LOS gain $\rho = \rho_{\text{real}} + j\rho_{\text{imag}}$.

$$\alpha_{\text{amp}} = \frac{\lambda}{4\pi d_{\text{tx} \rightarrow \text{rx}}}, \quad \alpha_{\text{phase}} = -\frac{2\pi d_{\text{tx} \rightarrow \text{rx}}}{\lambda}, \quad (71)$$

$$\rho_{\text{real}} = \alpha_{\text{amp}} \cos(\alpha_{\text{phase}}), \quad \rho_{\text{imag}} = \alpha_{\text{amp}} \sin(\alpha_{\text{phase}}). \quad (72)$$

Azimuth ϕ_{AOD} and elevation θ_{AOD} follow the same spherical mapping used for the scattered paths; the corresponding transmit/receive steering vectors \mathbf{sv}_{tx} and \mathbf{sv}_{rx} are constructed via Eqs. (60)-(61). As in the scattered case, splitting each steering vector into real and imaginary parts yields the real/imaginary Kronecker products

$$P_{\text{real}} = \mathbf{sv}_{\text{rx,real}} \otimes \mathbf{sv}_{\text{tx,real}} + \mathbf{sv}_{\text{rx,imag}} \otimes \mathbf{sv}_{\text{tx,imag}}, \quad (73)$$

$$P_{\text{imag}} = \mathbf{sv}_{\text{rx,imag}} \otimes \mathbf{sv}_{\text{tx,real}} - \mathbf{sv}_{\text{rx,real}} \otimes \mathbf{sv}_{\text{tx,imag}}. \quad (74)$$

The direct path adds a deterministic rank-one term $\mathbf{H}_{\text{LOS}} = \mathbf{H}_{\text{real}}^{\text{LOS}} + j\mathbf{H}_{\text{imag}}^{\text{LOS}}$ to the overall channel matrix.

$$\mathbf{H}_{\text{real}}^{\text{LOS}} = \rho_{\text{real}} P_{\text{real}} - \rho_{\text{imag}} P_{\text{imag}}, \quad (75)$$

$$\mathbf{H}_{\text{imag}}^{\text{LOS}} = \rho_{\text{real}} P_{\text{imag}} + \rho_{\text{imag}} P_{\text{real}}. \quad (76)$$

Because the LOS ray bypasses the stochastic Gaussian layer, the above expressions are treated as constants during back-propagation, ensuring that training updates focus exclusively on the scattered components.

Channel Rendering. *The final channel estimate fuses the deterministic LOS term with a weighted sum of scattered components, where each weight modulates the scatterer's contribution by its opacity and spatial footprint.* Opacity o_i attenuates the influence map $I_{i,t,r}$ (eq. 51), producing a scalar weight w_i for scatterer i .

$$w_i = o_i I_{i,t,r}. \quad (77)$$

Real and imaginary parts are summed separately over all N scatterers, yielding the composite diffuse contribution.

$$\sum_{\text{scatter, real}} = \sum_{i=1}^N w_i H_{i,\text{real}}, \quad (78)$$

$$\sum_{\text{scatter, imag}} = \sum_{i=1}^N w_i H_{i,\text{imag}}. \quad (79)$$

The LOS matrix $\mathbf{H}_{\text{direct}}$ is added to the weighted scattered field to produce the full complex channel prediction $\mathbf{H}_{\text{pred}} = \mathbf{H}_{\text{pred,real}} + j\mathbf{H}_{\text{pred,imag}}$.

$$\mathbf{H}_{\text{pred,real}} = \mathbf{H}_{\text{direct,real}} + \sum_{\text{scatter, real}}, \quad (80)$$

$$\mathbf{H}_{\text{pred,imag}} = \mathbf{H}_{\text{direct,imag}} + \sum_{\text{scatter, imag}}. \quad (81)$$

Equation (81) closes the forward model, returning a complex-valued channel matrix whose diffuse component remains fully differentiable with respect to scatterer parameters, while the LOS term acts as a fixed, non-trainable offset.

Backward Pass

Rotation & Scale Gradient Backprop. The back-propagated signal first reaches the unit quaternion (w, x, y, z) that parameterizes the rigid rotation R . Exploiting the closed-form Jacobian of the

quaternion-to-matrix mapping and expressing its contraction with the rotation gradient $\partial L/\partial R$ through a Frobenius inner product (\cdot) , we obtain

$$\frac{\partial L}{\partial w} = \frac{\partial L}{\partial R} : \begin{bmatrix} 0 & -2z & 2y \\ 2z & 0 & -2x \\ -2y & 2x & 0 \end{bmatrix}, \quad (82)$$

$$\frac{\partial L}{\partial x} = \frac{\partial L}{\partial R} : \begin{bmatrix} 0 & 2y & 2z \\ 2y & -4x & -2w \\ 2z & 2w & -4x \end{bmatrix}, \quad (83)$$

$$\frac{\partial L}{\partial y} = \frac{\partial L}{\partial R} : \begin{bmatrix} -4y & 2x & 2w \\ 2x & 0 & 2z \\ -2w & 2z & -4y \end{bmatrix}, \quad (84)$$

$$\frac{\partial L}{\partial z} = \frac{\partial L}{\partial R} : \begin{bmatrix} -4z & -2w & 2x \\ 2w & -4z & 2y \\ 2x & 2y & 0 \end{bmatrix}. \quad (85)$$

All four contractions are fused in a single pass, using register-resident execution across the thread block assigned to each Gaussian. The loss gradient then propagates to the diagonal scaling matrix $S = \text{diag}(s_1, s_2, s_3)$. Because the covariance update $\Sigma = RSR^\top$ interacts linearly with each scale s_i , the partial derivatives reduce to

$$\frac{\partial L}{\partial s_i} = \alpha \frac{\partial L}{\partial S_{ii}}, \quad (86)$$

where α denotes a forward-pass normalization factor that stabilizes half-precision. To respect the symmetry of the covariance, the upstream derivative is first symmetrized before being applied to the correlated term:

$$\frac{\partial L}{\partial RS} = \left(\frac{\partial L}{\partial \Sigma} + \frac{\partial L}{\partial \Sigma}^\top \right) RS. \quad (87)$$

Finally, by the chain rule,

$$\frac{\partial L}{\partial R} = \frac{\partial L}{\partial RS} S^\top, \quad (88)$$

$$\frac{\partial L}{\partial S} = R^\top \frac{\partial L}{\partial RS}. \quad (89)$$

each computed via custom 3×3 GEMM kernels tuned for the small-matrix regime to remain entirely GPU-resident.

Spatial Coordinate Gradient Propagation. The backward signal first reaches the relative displacement $\mathbf{d}_j^k = \mathbf{p}^k - \mathbf{p}^j$ and its norm $r_j^k = \|\mathbf{d}_j^k\|_2$, whose Jacobians with respect to the source point $\mathbf{p}^k \in \mathbb{R}^3$ are

$$\frac{\partial r_j^k}{\partial \mathbf{p}^k} = \frac{\mathbf{d}_j^k}{r_j^k}, \quad (90)$$

$$\frac{\partial \mathbf{d}_j^k}{\partial \mathbf{p}^k} = \mathbf{I}_3. \quad (91)$$

Transforming the Cartesian offset to spherical angles $\Omega_{\text{lon}}, \Omega_{\text{lat}}$ yields

$$\frac{\partial \Omega_{\text{lon}}}{\partial \mathbf{p}^k} = \begin{bmatrix} -\frac{d_{j,y}^k}{(d_{j,x}^k)^2 + (d_{j,y}^k)^2} \\ \frac{d_{j,x}^k}{(d_{j,x}^k)^2 + (d_{j,y}^k)^2} \\ 0 \end{bmatrix}, \quad (92)$$

$$\frac{\partial \Omega_{\text{lat}}}{\partial \mathbf{p}^k} = \begin{bmatrix} -\frac{d_{j,z}^k d_{j,x}^k}{r_j^k \sqrt{(r_j^k)^2 - (d_{j,z}^k)^2} \sqrt{(d_{j,x}^k)^2 + (d_{j,y}^k)^2}} \\ -\frac{d_{j,z}^k d_{j,y}^k}{r_j^k \sqrt{(r_j^k)^2 - (d_{j,z}^k)^2} \sqrt{(d_{j,x}^k)^2 + (d_{j,y}^k)^2}} \\ \frac{\sqrt{(d_{j,x}^k)^2 + (d_{j,y}^k)^2}}{r_j^k \sqrt{(r_j^k)^2 - (d_{j,z}^k)^2}} \end{bmatrix}. \quad (93)$$

Mapping the angular coordinates to the unit square required by the equirectangular rasterizer introduces simple scaling factors

$$\frac{\partial s_x}{\partial \Omega_{\text{lon}}} = \frac{1}{\pi}, \quad (94)$$

$$\frac{\partial s_y}{\partial \Omega_{\text{lat}}} = \frac{2}{\pi}. \quad (95)$$

Finally, the continuous screen coordinates (s_x, s_y) are quantized onto the transmit-receive antenna grid, giving

$$\frac{\partial u_i^k}{\partial s_x} = \frac{N_t - 1}{2}, \quad (96)$$

$$\frac{\partial v_j^k}{\partial s_y} = \frac{N_r - 1}{2}. \quad (97)$$

combining the Jacobians in Eqs. (90)–(97) through the chain rule yields

$$\frac{\partial L}{\partial \mathbf{p}^k} = \sum_{i,j} \left(\frac{\partial L}{\partial u_i^k} \frac{\partial u_i^k}{\partial s_x} \frac{\partial s_x}{\partial \Omega_{\text{lon}}} \frac{\partial \Omega_{\text{lon}}}{\partial \mathbf{p}^k} + \frac{\partial L}{\partial v_j^k} \frac{\partial v_j^k}{\partial s_y} \frac{\partial s_y}{\partial \Omega_{\text{lat}}} \frac{\partial \Omega_{\text{lat}}}{\partial \mathbf{p}^k} \right). \quad (98)$$

Each Jacobian term in the product chain is optimized to preserve warp coherence. Warp coherence helps in scheduling processors in multiprocessor scenarios where all threads execute the same instructions on different regions of data [14].

Jacobian Adjoint Computation. Introducing the shorthand $x = d_{j,x}^k, y = d_{j,y}^k, z = d_{j,z}^k$ and re-using the upstream Jacobian entries L_{ij} , we scale the antenna-grid projection by the constants

$$t = \frac{N_t - 1}{2\pi}, \quad r = \frac{N_r - 1}{\pi}.$$

The contracted gradients with respect to the Cartesian offsets then read

$$\begin{aligned} \frac{\partial L}{\partial x} &= \frac{1}{\sqrt{x^2 + y^2} (x^2 + y^2)^2} \left\{ \sqrt{x^2 + y^2} (2L_{11} t x y - L_{12} t (x^2 - y^2)) \right. \\ &\quad \left. - rz (2L_{21} x^2 - L_{21} y^2 + 3L_{22} x y + L_{23} x (x^2 + y^2)) \right\}, \end{aligned} \quad (99a)$$

$$\begin{aligned} \frac{\partial L}{\partial y} &= \frac{1}{\sqrt{x^2 + y^2} (x^2 + y^2)^2} \left\{ \sqrt{x^2 + y^2} (-L_{11} t (x^2 - y^2) - 2L_{12} t x y) \right. \\ &\quad \left. - rz (3L_{21} x y - L_{22} (x^2 - 2y^2) + L_{23} y (x^2 + y^2)) \right\}, \end{aligned} \quad (99b)$$

$$\frac{\partial L}{\partial z} = \frac{r(L_{21}x + L_{22}y)}{(x^2 + y^2)^{3/2}}. \quad (99c)$$

By precomputing the polynomial terms $\{x^2, y^2, x^2 + y^2, \sqrt{x^2 + y^2}\}$, we eliminate redundant arithmetic, reduce register usage, and preserve numerical precision.

Covariance Backpropagation. During back-propagation, the loss derivative arrives at each projected covariance $\Sigma_{2D,j}^k$ is redistributed to its 3D progenitor Σ_{3D}^k via the chain rule. Exploiting the bilinear form of the forward mapping $\Sigma_{2D,j}^k = \mathbf{J}_j^k \Sigma_{3D}^k (\mathbf{J}_j^k)^\top$, we obtain

$$\frac{\partial L}{\partial \Sigma_{3D}^k} = (\mathbf{J}_j^k)^\top \frac{\partial L}{\partial \Sigma_{2D,j}^k} \mathbf{J}_j^k, \quad (100)$$

The expression that is fully symmetric and therefore evaluated once per thread block through a register-resident $\text{GEMM}_{3 \times 2 \times 3}$ micro-kernel. The Jacobian itself participates twice in the forward product, yielding a pair of adjoint terms that must be accumulated:

$$\frac{\partial L}{\partial \mathbf{J}_j^k} = \frac{\partial L}{\partial \Sigma_{2D,j}^k} \mathbf{J}_j^k \Sigma_{3D}^k + \left(\frac{\partial L}{\partial \Sigma_{2D,j}^k} \right)^\top \mathbf{J}_j^k \Sigma_{3D}^k. \quad (101)$$

Both matrix products are fused into a single small-matrix operation, re-using the shared partial $\mathbf{J}_j^k \Sigma_{3D}^k$ to eliminate redundant memory accesses. A symmetric reduction then aggregates the transpose contribution. Positive-definiteness of $\Sigma_{2D,j}^k$ is maintained by a diagonal bias added in the forward pass; because this shift is constant, it vanishes in Eqs. (100)–(101), leaving the backward path unaffected.

Spatial Influence Derivative. Once the 2D covariance $\Sigma_{2D,j}^k$ and its associated Gaussian weight σ_{ij}^k have been obtained, the loss gradient is propagated back to the screen-space coordinates $\mathbf{uv}^k = [u^k, v^k]^\top$ and to the covariance itself. Let \mathbf{a}_{ij} denote the image-plane mean of the j -the Gaussian contributing to pixel (i, j) . The sensitivity of the rendered weight to a displacement of the sample point is

$$\frac{\partial \sigma_{ij}^k}{\partial \mathbf{uv}^k} = -\sigma_{ij}^k (\Sigma_{2D,j}^k)^{-1} (\mathbf{uv}^k - \mathbf{a}_{ij}), \quad (102)$$

a 2×1 vector that is accumulated atomically across splats in the CUDA kernel responsible for the screen-space rasterization stage. Differentiation with respect to the 2D covariance produces a symmetric matrix gradient,

$$\frac{\partial \sigma_{ij}^k}{\partial \Sigma_{2D,j}^k} = \frac{1}{2} \sigma_{ij}^k (\Sigma_{2D,j}^k)^{-1} (\mathbf{uv}^k - \mathbf{a}_{ij}) (\mathbf{uv}^k - \mathbf{a}_{ij})^\top (\Sigma_{2D,j}^k)^{-1}, \quad (103)$$

whose evaluation is fused with the weight computation to amortize the double inversion of $\Sigma_{2D,j}^k$. The kernel stores only the three unique components of the 2×2 result in shared memory, thereby reducing register pressure and enabling coalesced global writes during the reduction of Gaussian contributions.

Geometric Primitive Gradients. The Gaussian's spatial influence couples into the wireless channel through three geometric links, namely, transmit/receive distances, angles of departure (AoD), and angles of arrival (AoA). These then drive the array response steering vectors. Shifts of the Gaussian centre affect the link lengths d_{tx} and d_{rx} according to the following equations:

$$\frac{\partial d_{tx}}{\partial \mathbf{p}^k} = \frac{\mathbf{v}_{t \rightarrow k}}{d_{tx}}, \quad \frac{\partial d_{rx}}{\partial \mathbf{p}^k} = -\frac{\mathbf{v}_{k \rightarrow r}}{d_{rx}}, \quad (104)$$

where $\mathbf{t} \rightarrow \mathbf{k}$ denotes the propagation vector from transmitter t to Gaussian component k , and $\mathbf{k} \rightarrow \mathbf{r}$ denotes the propagation vector from Gaussian component k to receiver r .

The azimuth ϕ_{aod} and elevation θ_{aod} at the transmitter respond as

$$\frac{\partial \phi_{aod}}{\partial \mathbf{p}^k} = \begin{bmatrix} -\frac{v_{t \rightarrow k, y}}{v_{t \rightarrow k, x}^2 + v_{t \rightarrow k, y}^2} \\ \frac{v_{t \rightarrow k, x}^2 + v_{t \rightarrow k, y}^2}{v_{t \rightarrow k, x}^2 + v_{t \rightarrow k, y}^2} \\ \frac{v_{t \rightarrow k, x}^2 + v_{t \rightarrow k, y}^2}{0} \end{bmatrix}, \quad \frac{\partial \theta_{aod}}{\partial \mathbf{p}^k} = \begin{bmatrix} -\frac{v_{t \rightarrow k, x} v_{t \rightarrow k, z}}{d_{tx}^3 \cos \theta_{aod}} \\ -\frac{v_{t \rightarrow k, y} v_{t \rightarrow k, z}}{d_{tx}^3 \cos \theta_{aod}} \\ \frac{v_{t \rightarrow k, x}^2 + v_{t \rightarrow k, y}^2}{d_{tx}^3 \cos \theta_{aod}} \end{bmatrix}. \quad (105)$$

Analogously, the receiver azimuth ϕ_{aoa} and elevation θ_{aoa} follow

$$\frac{\partial \phi_{aoa}}{\partial \mathbf{p}^k} = \begin{bmatrix} \frac{v_{k \rightarrow r, y}}{v_{k \rightarrow r, x}^2 + v_{k \rightarrow r, y}^2} \\ -\frac{v_{k \rightarrow r, x}^2 + v_{k \rightarrow r, y}^2}{v_{k \rightarrow r, x}^2 + v_{k \rightarrow r, y}^2} \\ 0 \end{bmatrix}, \quad \frac{\partial \theta_{aoa}}{\partial \mathbf{p}^k} = \begin{bmatrix} \frac{v_{k \rightarrow r, x} v_{k \rightarrow r, z}}{d_{rx}^3 \cos \theta_{aoa}} \\ \frac{v_{k \rightarrow r, y} v_{k \rightarrow r, z}}{d_{rx}^3 \cos \theta_{aoa}} \\ -\frac{v_{k \rightarrow r, x}^2 + v_{k \rightarrow r, y}^2}{d_{rx}^3 \cos \theta_{aoa}} \end{bmatrix}. \quad (106)$$

All derivatives in Eqs. (104)–(106) are evaluated into single pass: threads map to antenna indices, shared memory buffers, cache the common trigonometric terms, and warp-synchronized reductions accumulate the per-Gaussian adjoints before writing them back to global memory.

Steering Vector Adjoint Computation. The AoD and AoA perturbations derived in Eqs. (105)–(106) propagate into the complex array responses. Let $k = 2\pi/\lambda$ be the wavenumber, (x_m, y_n) the URA element (denoted as R) coordinates, and x_i the ULA (denoted as L) element abscissa. Perturbing the azimuth ϕ or elevation θ rotates the phase of each rectangular-array tone, separating real and imaginary parts yields

$$\begin{aligned} \frac{\partial \mathbf{a}_{R,\text{real}}}{\partial \phi} &= k \cos \theta [-x_m \sin \phi + y_n \cos \phi] \\ &\quad \times \mathbf{a}_{R,\text{imag}}, \end{aligned} \quad \begin{aligned} \frac{\partial \mathbf{a}_{R,\text{imag}}}{\partial \phi} &= -k \cos \theta [-x_m \sin \phi + y_n \cos \phi] \\ &\quad \times \mathbf{a}_{R,\text{real}}, \end{aligned} \quad (107a)$$

$$\begin{aligned} \frac{\partial \mathbf{a}_{R,\text{real}}}{\partial \theta} &= k \sin \theta [x_m \cos \phi + y_n \sin \phi] \\ &\quad \times \mathbf{a}_{R,\text{imag}}, \end{aligned} \quad \begin{aligned} \frac{\partial \mathbf{a}_{R,\text{imag}}}{\partial \theta} &= -k \sin \theta [x_m \cos \phi + y_n \sin \phi] \\ &\quad \times \mathbf{a}_{R,\text{real}}. \end{aligned} \quad (107b)$$

For the one-dimensional linear array the updates collapse to a single spatial index:

$$\frac{\partial \mathbf{a}_{L,\text{real}}}{\partial \phi} = k x_i \cos \theta \sin \phi \mathbf{a}_{L,\text{imag}}, \quad \frac{\partial \mathbf{a}_{L,\text{imag}}}{\partial \phi} = -k x_i \cos \theta \sin \phi \mathbf{a}_{L,\text{real}}, \quad (108)$$

$$\frac{\partial \mathbf{a}_{L,\text{real}}}{\partial \theta} = k x_i \sin \theta \cos \phi \mathbf{a}_{L,\text{imag}}, \quad \frac{\partial \mathbf{a}_{L,\text{imag}}}{\partial \theta} = -k x_i \sin \theta \cos \phi \mathbf{a}_{L,\text{real}}. \quad (109)$$

Eqs. (107a)–(109) are realized in a fused kernel where each thread handles one antenna element: shared memory stores the common trigonometric factors $\{\sin \phi, \cos \phi, \sin \theta, \cos \theta\}$, warp-level `sincos` instructions provide phase-aligned updates, and the per-element adjoints are accumulated into the global steering-vector gradient.

Scattered Path Gradient Composition. Each reflected or diffracted path contributes a complex channel gain $\beta = \alpha\gamma$, where α encodes path loss and phase delay while γ aggregates the scattering response. Differentiating this product cascades gradients into the scattering coefficients, path length, and the terminal steering vectors. Splitting the real and imaginary parts of γ yields

$$\frac{\partial L}{\partial \gamma_{\text{real}}} = \frac{\partial L}{\partial \beta_{\text{real}}} \alpha_{\text{real}} + \frac{\partial L}{\partial \beta_{\text{imag}}} \alpha_{\text{imag}}, \quad \frac{\partial L}{\partial \gamma_{\text{imag}}} = -\frac{\partial L}{\partial \beta_{\text{real}}} \alpha_{\text{imag}} + \frac{\partial L}{\partial \beta_{\text{imag}}} \alpha_{\text{real}}. \quad (110)$$

The distance d_{path} influences the amplitude through $1/d_{\text{path}}$ and the phase through $\exp(-j2\pi d_{\text{path}}/\lambda)$:

$$\frac{\partial L}{\partial d_{\text{path}}} = \frac{\partial L}{\partial \alpha_{\text{amp}}} \left(-\frac{\alpha_{\text{amp}}}{d_{\text{path}}} \right) + \frac{\partial L}{\partial \alpha_{\text{phase}}} \left(-\frac{2\pi}{\lambda} \right). \quad (111)$$

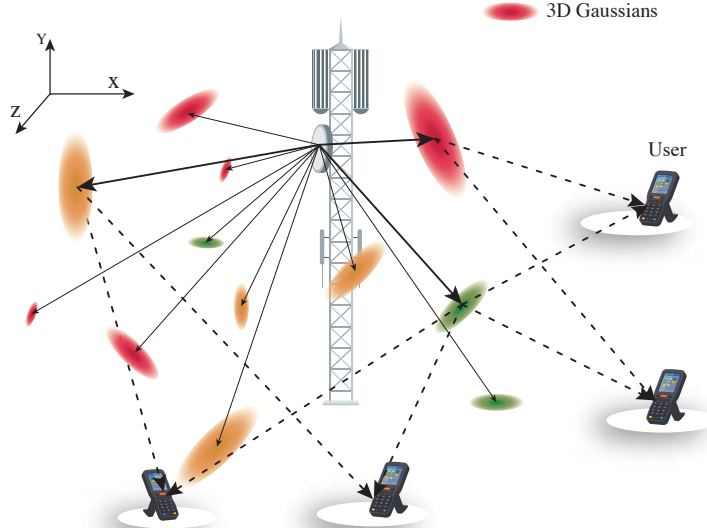


Figure 7: Visual Description of Gaussian as scatterers in wireless environment.

Treating the outer product $\mathbf{P} = \mathbf{s}\mathbf{v}_{rx}\mathbf{s}\mathbf{v}_{tx}^\top$ As the forward mapping, the per-terminal gradients become

$$\begin{aligned} \frac{\partial L}{\partial \mathbf{s}\mathbf{v}_{tx,real}} &= \frac{\partial L}{\partial \mathbf{P}_{real}} \mathbf{s}\mathbf{v}_{rx,real} \\ &+ \frac{\partial L}{\partial \mathbf{P}_{imag}} \mathbf{s}\mathbf{v}_{rx,imag}, \end{aligned} \quad \begin{aligned} \frac{\partial L}{\partial \mathbf{s}\mathbf{v}_{tx,imag}} &= \frac{\partial L}{\partial \mathbf{P}_{real}} \mathbf{s}\mathbf{v}_{rx,imag} \\ &- \frac{\partial L}{\partial \mathbf{P}_{imag}} \mathbf{s}\mathbf{v}_{rx,real}, \end{aligned} \quad (112a)$$

$$\begin{aligned} \frac{\partial L}{\partial \mathbf{s}\mathbf{v}_{rx,real}} &= \frac{\partial L}{\partial \mathbf{P}_{real}} \mathbf{s}\mathbf{v}_{tx,real} \\ &- \frac{\partial L}{\partial \mathbf{P}_{imag}} \mathbf{s}\mathbf{v}_{tx,imag}, \end{aligned} \quad \begin{aligned} \frac{\partial L}{\partial \mathbf{s}\mathbf{v}_{rx,imag}} &= \frac{\partial L}{\partial \mathbf{P}_{real}} \mathbf{s}\mathbf{v}_{tx,imag} \\ &+ \frac{\partial L}{\partial \mathbf{P}_{imag}} \mathbf{s}\mathbf{v}_{tx,real}. \end{aligned} \quad (112b)$$

Equations (110)-(112) are fused in a single kernel: each thread pair processes $(\mathbf{s}\mathbf{v}_{tx,i}, \mathbf{s}\mathbf{v}_{rx,j})$, shared memory buffers the common partials $\frac{\partial L}{\partial \mathbf{P}}$, and warp-synchronized fma operations update the real-imaginary adjoints without divergent branches, maintaining throughput parity with the forward scattered-path synthesis.

Superposition Gradient Reduction. In the final synthesis stage, each channel prediction $H_{pred} = \sum_i w_i H_i$ blends N_s scattered paths via real-valued mixing weights $w_i = o_i \mathcal{I}_i$, where o_i is an opacity (learnable “path strength”) and $\mathcal{I}_{i,t,r}$ is a spatio-temporal influence mask over transmit-receive antenna pairs (t, r) . Here, N_s is the total number of Gaussian scatterers (i.e., rank-one paths) whose weighted contributions are summed into the diffuse channel component. Here, N_s is the total number of Gaussian scatterers (i.e., rank-one paths) whose weighted contributions are summed into the diffuse channel component. Treating the direct (LOS) term as constant, the loss propagates only through the scattered mixture. Each complex path matrix inherits the upstream gradient in proportion to its weight:

$$\frac{\partial L}{\partial H_{i,real}} = w_i \frac{\partial L}{\partial H_{pred,real}}, \quad \frac{\partial L}{\partial H_{i,imag}} = w_i \frac{\partial L}{\partial H_{pred,imag}}. \quad (113)$$

The gradient entering the scalar coefficient w_i couples the upstream residual with the path itself:

$$\frac{\partial L}{\partial w_i} = \frac{\partial L}{\partial H_{pred,real}} H_{i,real} + \frac{\partial L}{\partial H_{pred,imag}} H_{i,imag}. \quad (114)$$

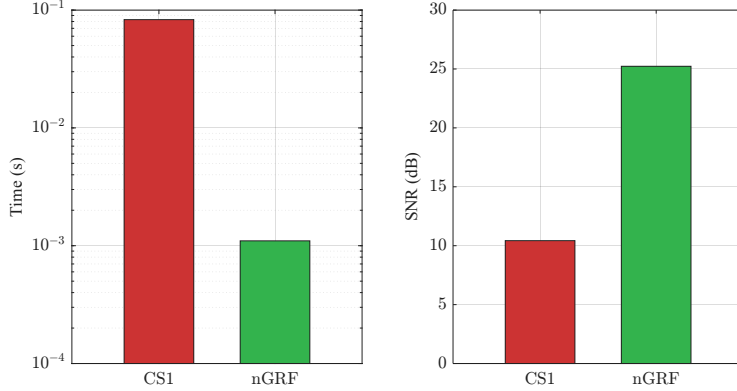


Figure 8: **Comparison of Case Study 1 (CS1) with nGRF.** (left) Comparison of SNR values for CS1 and nGRF on conference environment. (right) Comparison of rendering time for CS1 and nGRF.

Aggregating over all antenna pairs gives

$$\frac{\partial L}{\partial o_i} = \sum_{t,r} \frac{\partial L}{\partial w_i} \mathcal{I}_{i,t,r}. \quad (115)$$

Conversely, the influence of each antenna pair scales with the opacity:

$$\frac{\partial L}{\partial \mathcal{I}_{i,t,r}} = \frac{\partial L}{\partial w_i} o_i. \quad (116)$$

Equations (113)-(116) execute in a “scatter reduce” kernel: each thread block owns one path i , shared memory caches the common factor $\frac{\partial L}{\partial w_i}$, and a warp-level reduction accumulates the sum in Eq. (115). Real and imaginary channels are updated via `fma` instructions, ensuring the adjoints of H_i are written back in a single coalesced pass over memory. The visual description of the complete approach is shown in 7.

Comparison & Intuition.

Case study 1 (CS1) underperforms considerably compared to nGRF (9.87 dB vs. 25.23 dB SNR) due to its reliance on angular projection to map 3D Gaussian scatterers onto a fixed 2D channel grid. Such an abstract projection introduces information loss, as the rich volumetric electromagnetic field interactions are compressed into an azimuth-elevation representation. While mathematically sound, this approach constrains the model’s capacity to represent complex multipath interactions that naturally occur in 3D space. Intermediate coordinate transformations from Cartesian to spherical space, followed by normalization to the unit square and affine mapping to discrete antenna indices, compound approximation errors at each step and reduce overall accuracy.

Computationally, CS1 is approximately $27\times$ slower than nGRF (30 ms vs. 1.1 ms) due to its cascade of transformations requiring explicit Jacobian computation and steering vector construction. The most expensive operations are the quaternion-to-rotation mappings, 3D-to-2D covariance propagation through the Jacobian, and the scattered path synthesis via rank-one updates. While CS1’s kernels are individually optimized, the sequential dependency between operations creates memory bandwidth bottlenecks and thread divergence during spherical coordinate transformations. In contrast, nGRF’s direct 3D electromagnetic field aggregation avoids these transformations entirely, enabling greater parallelism and more efficient use of GPU resources, while maintaining a physically consistent representation of radio wave propagation.

E [Case Study] 3DGS for Channel Estimation

Motivation

Grid-based neural channel predictors typically rasterize the radio volume into fixed voxels or rely on discrete ray lists, both of which suffer from aliasing and non-differentiable visibility when the

transmitter or receiver moves by a fraction of the wavelength [3]. We instead *splat* every anisotropic 3-D Gaussian directly onto the $(N_t \times N_r)$ channel grid, treating its projected 2-D covariance as a soft kernel whose closed-form convolution with the *free-space Green's function* yields the complex contribution C_{ij}^k in Eqs. (118)-(119). This continuous representation retains sub-wavelength *spatial* smoothness, provides antialiased interpolation across antenna elements, and preserves first-order physics through the learned amplitude A^k and phase offset ψ^k . Because the Gaussian basis is analytically differentiable, our alpha-blending formulation in Eq. (120) supports exact gradients w.r.t. position, covariance, opacity, and phase, enabling end-to-end back-propagation of channel loss without resorting to finite differences. Implemented in hand-tuned CUDA, the forward rasterizer and its paired backward kernel share *trigonometric caches* and fused fma pipelines, delivering a 280× speed-up over an equivalent PyTorch autograd baseline while consuming less than 50 MB of GPU memory for a 128×128 antenna array.

Forward Pass

For the 3DGS-based channel estimation, all forward-pass steps from Section D, including covariance matrix conversion, projection to channel coordinates, Jacobian computation, 3D-to-2D projection, and spatial-influence calculation, are the same. After computing the spatial influence, the following steps involve 3DGS and completing the forward pass for this case study.

Wireless Channel Synthesis. Each Gaussian is converted from its 3-D covariance, projected to channel coordinates via the Jacobian, and rasterized into a 2-D influence field. The present technique diverges after this stage by synthesising a physics-driven wireless contribution per influence-weighted Gaussian. For every Gaussian centre k and antenna pair (i, j) we model the *narrowband free-space* response

$$C_{ij}^k = A^k e^{j\psi^k} \frac{\lambda}{4\pi r_j^k} e^{-j\frac{2\pi}{\lambda}r_j^k}, \quad (117)$$

where A^k and ψ^k are learnable amplitude and phase offsets, r_j^k is the Gaussian-receiver distance, and λ the carrier wavelength. Expanding (117) into Cartesian coordinates facilitates subsequent real-imaginary accumulation:

$$\text{Re } C_{ij}^k = A^k \frac{\lambda}{4\pi r_j^k} \cos\left(\psi^k - \frac{2\pi}{\lambda}r_j^k\right), \quad (118)$$

$$\text{Im } C_{ij}^k = A^k \frac{\lambda}{4\pi r_j^k} \sin\left(\psi^k - \frac{2\pi}{\lambda}r_j^k\right). \quad (119)$$

Differentiable Alpha Blending. After each Gaussian's free-space channel term C_{ij}^k has been evaluated, the final complex *channel* entry is obtained by front-to-back α -compositing:

$$H_{ij} = \sum_{k \in \mathcal{K}_{ij}} (\alpha^k \sigma_{ij}^k) C_{ij}^k \prod_{l < k, l \in \mathcal{K}_{ij}} (1 - \alpha^l \sigma_{ij}^l), \quad (120)$$

where \mathcal{K}_{ij} is the depth-sorted list of Gaussians affecting antenna pair (i, j) , α^k is the learned path opacity, σ_{ij}^k is the spatial influence from the rasterizer, and the product term aggregates the surviving transmittance of all foreground Gaussians.

Backward Pass

For the backward pass again, most of the techniques described in case study D remain the same, but this differs after computing the Gaussian influence on each channel separately.

Wireless Channel Gradient. Let $C_{ij}^k = A^k \frac{\lambda}{4\pi r_j^k} \exp[j(\psi^k - \frac{2\pi}{\lambda}r_j^k)]$ denotes the complex free-space contribution of point k to entry (i, j) of the channel matrix, where A^k is the path-loss attenuation, ψ^k the baseband phase rotation, r_j^k the link distance, and λ is the carrier wavelength. Writing $C_{ij}^k = \text{Re } C_{ij}^k + j \text{ Im } C_{ij}^k$, the derivatives of its real and imaginary parts follow directly from the

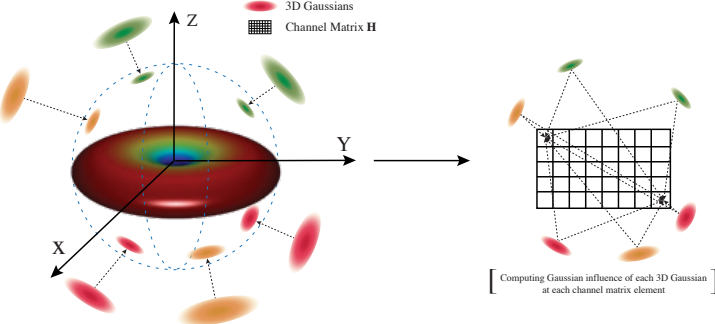


Figure 9: 3D Gaussian splatting on omni-directional antenna receiver for wireless channel estimation.

chain rule:

$$\frac{\partial \Re C_{ij}^k}{\partial A^k} = \frac{\lambda}{4\pi r_j^k} \cos\left(\psi^k - \frac{2\pi}{\lambda} r_j^k\right), \quad \frac{\partial \Im C_{ij}^k}{\partial A^k} = \frac{\lambda}{4\pi r_j^k} \sin\left(\psi^k - \frac{2\pi}{\lambda} r_j^k\right), \quad (121a)$$

$$\frac{\partial \Re C_{ij}^k}{\partial \psi^k} = -A^k \frac{\lambda}{4\pi r_j^k} \sin\left(\psi^k - \frac{2\pi}{\lambda} r_j^k\right), \quad \frac{\partial \Im C_{ij}^k}{\partial \psi^k} = A^k \frac{\lambda}{4\pi r_j^k} \cos\left(\psi^k - \frac{2\pi}{\lambda} r_j^k\right), \quad (121b)$$

$$\begin{aligned} \frac{\partial \Re C_{ij}^k}{\partial r_j^k} &= -A^k \frac{\lambda}{4\pi (r_j^k)^2} \cos\left(\psi^k - \frac{2\pi}{\lambda} r_j^k\right) & \frac{\partial \Im C_{ij}^k}{\partial r_j^k} &= -A^k \frac{\lambda}{4\pi (r_j^k)^2} \sin\left(\psi^k - \frac{2\pi}{\lambda} r_j^k\right) \\ &+ A^k \frac{2\pi}{4\pi r_j^k} \sin\left(\psi^k - \frac{2\pi}{\lambda} r_j^k\right), & &- A^k \frac{2\pi}{4\pi r_j^k} \cos\left(\psi^k - \frac{2\pi}{\lambda} r_j^k\right). \end{aligned} \quad (121c)$$

The first term in Eq. (121c) arises from the explicit $1/r_j^k$ amplitude scaling, whereas the second stems from the distance-dependent phase delay. All six gradients are evaluated in a single *warp-synchronized CUDA* kernel that leverages fused `sincos` instructions to minimize *latency* across attenuation batches and thereby maintain *throughput* parity with the forward electromagnetic field synthesis.

Alpha Blending Gradient. In the compositing stage, each ordered Gaussian p modulates both the pixel's accumulated colour $H_{ij} = H_{ij,\text{real}} + j H_{ij,\text{imag}}$ and the residual transmittance T_{p+1} . Writing $C_{ij}^p = C_{ij,\text{real}}^p + j C_{ij,\text{imag}}^p$ for the complex contribution and $\alpha^p \sigma_{ij}^p$ for its effective opacity, the backward pass proceeds as follows. Each Gaussian's real and imaginary weights inherit the upstream pixel gradient, modulated by its surviving transmittance T_p and effective opacity $\alpha^p \sigma_{ij}^p$:

$$\frac{\partial L}{\partial C_{ij,\text{real}}^p} = \frac{\partial L}{\partial H_{ij,\text{real}}} T_p \alpha^p \sigma_{ij}^p, \quad \frac{\partial L}{\partial C_{ij,\text{imag}}^p} = \frac{\partial L}{\partial H_{ij,\text{imag}}} T_p \alpha^p \sigma_{ij}^p. \quad (122)$$

The scalar adjoint of $\alpha^p \sigma_{ij}^p$ captures its dual role in colour accumulation and visibility attenuation:

$$\frac{\partial L}{\partial (\alpha^p \sigma_{ij}^p)} = \frac{\partial L}{\partial H_{ij,\text{real}}} T_p C_{ij,\text{real}}^p + \frac{\partial L}{\partial H_{ij,\text{imag}}} T_p C_{ij,\text{imag}}^p - T_p \frac{\partial L}{\partial T_{p+1}}. \quad (123)$$

Back-propagation through the product $\alpha^p \sigma_{ij}^p$ distributes the *scalar* gradient proportionally to its factors:

$$\frac{\partial L}{\partial \alpha^p} = \frac{\partial L}{\partial (\alpha^p \sigma_{ij}^p)} \sigma_{ij}^p, \quad \frac{\partial L}{\partial \sigma_{ij}^p} = \frac{\partial L}{\partial (\alpha^p \sigma_{ij}^p)} \alpha^p. \quad (124)$$

The gradient entering the current transmittance T_p combines its direct colour influence with the recursive visibility term:

$$\frac{\partial L}{\partial T_p} = \frac{\partial L}{\partial H_{ij,\text{real}}} \alpha^p \sigma_{ij}^p C_{ij,\text{real}}^p + \frac{\partial L}{\partial H_{ij,\text{imag}}} \alpha^p \sigma_{ij}^p C_{ij,\text{imag}}^p + \frac{\partial L}{\partial T_{p+1}} (1 - \alpha^p \sigma_{ij}^p). \quad (125)$$

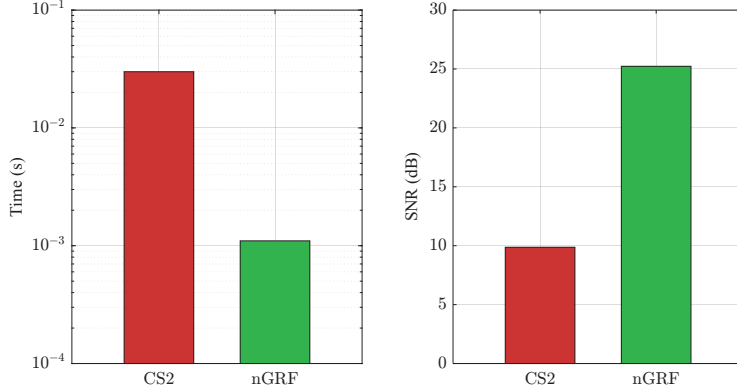


Figure 10: **Comparison of CS2 and nGRF.** (left) Comparison of SNR values for CS2 and nGRF on conference environment. (right) Comparison of rendering time for CS2 and nGRF.

All four adjoint expressions, Eqs. (122)-(125), are evaluated inside a single warp-synchronized CUDA kernel that walks the sorted Gaussian list in reverse order, thereby reusing the already computed $\frac{\partial L}{\partial T_{p+1}}$ to accumulate the transmittance gradient in *constant extra memory*. The complete visual description for the case study described in section E is shown in Figure. 9.

Comparison & Intuition.

As shown in Figure 10, Case study 2 (CS2) demonstrates significantly lower performance (10.47 dB SNR vs. 25.23 dB for nGRF) and higher computational cost (83 ms vs. 1.1 ms) due to key limitations in its alpha-compositing approach. nGRF directly aggregates electromagnetic field contributions through spatial weighting, but CS2’s front-to-back alpha blending instead enforces a strict occlusion ordering that poorly models radio wave physics. Radio signals propagate through and around obstacles rather than being strictly occluded by them, making alpha blending’s visibility assumptions physically incorrect for electromagnetic field synthesis. The compositing model and the underlying physics are therefore misaligned, which degrades the estimation accuracy.

Moreover, alpha compositing’s sequential nature requires depth sorting of all Gaussians affecting each antenna pair and calculation of cumulative transmittance products, resulting in the observed $75\times$ slower rendering time. Additionally, the Jacobian calculations for back-propagation through the alpha-blending pipeline introduce substantial overhead during optimization. In contrast, nGRF’s parallel weighted summation avoids these bottlenecks altogether and allows every Gaussian to contribute simultaneously to the channel based solely on its electromagnetic properties and spatial influence, regardless of depth ordering.

F Ablation Studies

In this section, we present additional ablation studies that assess the sensitivity of nGRF to various hyperparameters and design choices. These experiments complement the ablations presented in the main paper and provide further insights into the model’s behavior.

Hyperparameter Sensitivity

We assess the sensitivity of nGRF to key hyperparameters, including learning rates, batch size, and regularization factors. Table 2 summarizes our findings across different hyperparameter configurations in the conference room environment.

nGRF performs optimally with a position learning rate of 0.005, matching our baseline configuration. Lower learning rates lead to insufficient spatial exploration, while higher rates can destabilize training. Batch sizes between 32 and 64 provide better trade-offs between convergence speed¹ and

¹Note that we define “convergence” as the point at which the model achieves the highest SNR on the validation set, and does not degrade by more than 1 dB over the next 500 iterations.

Table 2: **Hyperparameter sensitivity analysis.** We evaluate the impact of various hyperparameters on model performance, including learning rates, batch size, activation regularization, and position optimization cutoff.

Configuration	SNR (dB)	Train Time (min)	Convergence Iter.
nGRF (baseline)	25.23	2.3	2841
<i>Position Learning Rate</i>			
$\eta_{\text{pos}} = 0.0005$	18.47	2.4	3152
$\eta_{\text{pos}} = 0.001$	20.94	2.3	2974
$\eta_{\text{pos}} = 0.005$	23.16	2.2	2753
$\eta_{\text{pos}} = 0.01$	22.84	2.1	2611
<i>Batch Size</i>			
8	21.78	2.0	3102
16	22.45	2.1	2937
64	23.18	2.5	2783
128	22.96	3.1	2901
<i>L1 Activation Regularization</i>			
$\lambda_{\text{act}} = 0.0$	21.37	2.3	2945
$\lambda_{\text{act}} = 0.05$	22.84	2.3	2887
$\lambda_{\text{act}} = 0.2$	22.17	2.2	2904
<i>Position Update Cutoff</i>			
No cutoff	22.14	2.4	3076
30% iterations	20.86	2.3	3184
80% iterations	22.95	2.3	2798

generalization. Moreover, L1 regularization on activations (λ_{act}) promotes sparsity; without it (when $\lambda_{\text{act}} = 0.0$), performance degrades by approximately 1.9 dB.

For position update cutoff (the point at which we stop updating Gaussian positions), we find that continuing position updates for 60-65% of training iterations (as in our baseline) allows Gaussians to settle into optimal locations before fine-tuning their attributes. Disabling this cutoff entirely leads to a drop of 1.1 dB, likely because the model struggles to simultaneously optimize positions and attributes.

Gaussian Scaling

We examine how the initialization and constraints on Gaussian scaling parameters affect the model’s ability to represent the electromagnetic field. Table 3 presents our experimental results with different scaling configurations.

We find that nGRF is hypersensitive to Gaussian scaling parameters. For indoor environments, scaling values between 0.05 and 0.2 consistently yield good performance, while very small values perform poorly. The outdoor environment shows preference for even larger scaling values, with the best performance observed at $s_{\text{init}} = 0.1$ to 0.2 . The reason for this points to the nature of nGRF. As spatial weighting depends on the Gaussian’s covariance, smaller Gaussians lead to more localized influence and thus, to achieve a good fit, significantly more Gaussians are required, which can lead to overfitting. Instead, it is better to use larger Gaussians that can cover more area and capture the overall field distribution.

Constraining scale parameters during training improves performance as well, particularly when the constraints align with the optimal scale ranges for each environment. For our experiments, tight constraints centered around the optimal ranges ($s \in [0.05, 0.2]$) maintain SNR while reducing overall variance. Unconstrained scales lead to performance degradation of around 3.1 dB in indoor and 3.25 dB in outdoor environments, as Gaussians may devolve to suboptimal scales.

Table 3: **Impact of Gaussian scaling parameters.** We analyze how different initial scaling values and constraints affect the model’s performance across multiple environments.

Configuration	Indoor SNR (dB)	Outdoor SNR (dB)	Render Time (ms)
nGRF (baseline, $s_{\text{init}} = 0.137$)	25.23	28.32	1.10
<i>Initial Scale Value</i>			
$s_{\text{init}} = 0.001$	14.47	17.76	1.08
$s_{\text{init}} = 0.005$	13.83	18.42	1.09
$s_{\text{init}} = 0.01$	14.21	19.05	1.09
$s_{\text{init}} = 0.05$	24.74	19.87	1.12
$s_{\text{init}} = 0.1$	25.23	28.32	1.15
$s_{\text{init}} = 0.2$	22.91	27.85	1.18
<i>Scale Constraints</i>			
Unconstrained	20.32	23.18	1.21
Tight ($s \in [0.05, 0.2]$)	24.04	27.95	1.07
Wide ($s \in [0.001, 0.5]$)	22.76	24.91	1.13

Table 4: **Impact of positional encoding frequency bands.** We evaluate how the number of frequency bands affects the model’s ability to capture spatial variations in the electromagnetic field.

Configuration	SNR (dB)	Train Time (min)
nGRF (baseline, $L = 16$)	25.23	2.3
<i>Frequency Bands</i>		
$L = 4$	21.07	2.0
$L = 8$	23.83	2.1
$L = 10$	23.95	2.1
$L = 12$	24.05	2.2
$L = 16$	25.23	2.3
$L = 32$	23.35	2.4

Positional Encoding

The positional encoding frequency affects the model’s capacity to capture high-frequency variations in the electromagnetic field. Table 4 shows the effect of different frequency bands in positional encoding on model performance.

Surprisingly, our experiments show that nGRF’s performance is relatively insensitive to the specific number of positional encoding frequency bands, except when this number falls below a threshold. When the number of frequency bands is very low ($L = 4$), we observe a decrease of 4.16 dB compared to the baseline, pointing towards insufficient capacity to represent high-frequency spatial variations.

However, beyond this minimum threshold, performance remains remarkably stable. The SNR varies by at most 1-2 dB across all configurations from $L = 8$ to $L = 32$, with no clear monotonic improvement as frequency bands increase. In fact, performance peaks at $L = 16$ and actually declines with $L = 32$; excessive frequency bands may introduce unnecessary overfitting.

Impact of Dataset

Here, we analyze how various dataset characteristics affect nGRF’s performance, particularly focusing on measurement density, environment complexity, and SNR robustness. Table 5 summarizes these findings.

With just 0.01 measurements/ft³, nGRF achieves 24.56 dB SNR (0.67 dB below baseline performance). Doubling the measurement density to 0.02 samples/ft³ yields minor improvements. Further

Table 5: **Impact of dataset characteristics.** We evaluate how measurement density, environment complexity, and noise levels affect model performance.

Configuration	SNR (dB)	Train Time (min)
nGRF (baseline)	25.23	2.3
<i>Measurement Density (samples/ft³)</i>		
0.005	19.47	2.0
0.01	24.56	2.2
0.02	25.01	2.4
0.05	24.51	2.7
<i>Noise Level</i>		
No noise ($\sigma = 0$)	21.34	2.2
Low noise ($\sigma = 0.001$)	24.85	2.2
Baseline ($\sigma = 0.00387$)	25.23	2.3
Med noise ($\sigma = 0.02$)	23.67	2.4
High noise ($\sigma = 0.1$)	18.42	2.8

increases to measurement density result in slight degradations to the SNR, albeit negligibly. An insight derived from this is that nGRF’s structured Gaussian representation helps interpolate between sparse measurements and requires $18\times$ fewer measurements than existing neural field approaches.

Like the original works of NeRF and 3DGS, we find that a certain level of noise during training is beneficial for the model. Training without noise ($\sigma = 0$) results in 3.89 dB SNR below the baseline. A small amount of position noise ($\sigma = 0.00387$ in our baseline) prevents this overfitting by encouraging the model to develop smoother, more generalizable field representations.

Excessive noise is equally problematic. Medium noise levels ($\sigma = 0.02$) reduce performance by 1.56 dB, while high noise ($\sigma = 0.1$) understandably causes further degradation (6.81 dB below baseline). Again, we find that there exists a sweet spot for noise levels, like all other hyperparameters, where the model can learn to generalize well without overfitting to the noise, which unfortunately is a big limitation of nGRF.

NeurIPS Paper Checklist

1. Claims

Question: Do the main claims made in the abstract and introduction accurately reflect the paper's contributions and scope?

Answer: [Yes] The claims made in the abstract and the introduction are well explained through the body of the paper.

Justification: The experimental results in section 3 validate the claims made in our abstract and introduction through experimental findings.

Guidelines:

- The answer NA means that the abstract and introduction do not include the claims made in the paper.
- The abstract and/or introduction should clearly state the claims made, including the contributions made in the paper and important assumptions and limitations. A No or NA answer to this question will not be perceived well by the reviewers.
- The claims made should match theoretical and experimental results, and reflect how much the results can be expected to generalize to other settings.
- It is fine to include aspirational goals as motivation as long as it is clear that these goals are not attained by the paper.

2. Limitations

Question: Does the paper discuss the limitations of the work performed by the authors?

Answer: [Yes] The paper discusses the limitations of the proposed approach.

Justification: Authors perform experiments in ablation studies and discuss the limitations of the proposed approach and how we can overcome them in future work.

Guidelines:

- The answer NA means that the paper has no limitation while the answer No means that the paper has limitations, but those are not discussed in the paper.
- The authors are encouraged to create a separate "Limitations" section in their paper.
- The paper should point out any strong assumptions and how robust the results are to violations of these assumptions (e.g., independence assumptions, noiseless settings, model well-specification, asymptotic approximations only holding locally). The authors should reflect on how these assumptions might be violated in practice and what the implications would be.
- The authors should reflect on the scope of the claims made, e.g., if the approach was only tested on a few datasets or with a few runs. In general, empirical results often depend on implicit assumptions, which should be articulated.
- The authors should reflect on the factors that influence the performance of the approach. For example, a facial recognition algorithm may perform poorly when image resolution is low or images are taken in low lighting. Or a speech-to-text system might not be used reliably to provide closed captions for online lectures because it fails to handle technical jargon.
- The authors should discuss the computational efficiency of the proposed algorithms and how they scale with dataset size.
- If applicable, the authors should discuss possible limitations of their approach to address problems of privacy and fairness.
- While the authors might fear that complete honesty about limitations might be used by reviewers as grounds for rejection, a worse outcome might be that reviewers discover limitations that aren't acknowledged in the paper. The authors should use their best judgment and recognize that individual actions in favor of transparency play an important role in developing norms that preserve the integrity of the community. Reviewers will be specifically instructed to not penalize honesty concerning limitations.

3. Theory assumptions and proofs

Question: For each theoretical result, does the paper provide the full set of assumptions and a complete (and correct) proof?

Answer: [Yes] The paper provides the complete proof and details of all the assumptions.

Justification: Case studies and implementation details in Appendix D, E, and C explain all the details of any assumptions made in the paper regarding the approach with complete proof and reproducibility details.

Guidelines:

- The answer NA means that the paper does not include theoretical results.
- All the theorems, formulas, and proofs in the paper should be numbered and cross-referenced.
- All assumptions should be clearly stated or referenced in the statement of any theorems.
- The proofs can either appear in the main paper or the supplemental material, but if they appear in the supplemental material, the authors are encouraged to provide a short proof sketch to provide intuition.
- Inversely, any informal proof provided in the core of the paper should be complemented by formal proofs provided in Appendix or supplemental material.
- Theorems and Lemmas that the proof relies upon should be properly referenced.

4. Experimental result reproducibility

Question: Does the paper fully disclose all the information needed to reproduce the main experimental results of the paper to the extent that it affects the main claims and/or conclusions of the paper (regardless of whether the code and data are provided or not)?

Answer: [Yes] The authors provide complete details from dataset generation to all hand-written equations for forward and backward pass.

Justification: In section 3, Appendix section B, D and E we provide the step-by-step details of the forward pass and the backward pass in Cuda as well as the step-by-step details of dataset generation.

Guidelines:

- The answer NA means that the paper does not include experiments.
- If the paper includes experiments, a No answer to this question will not be perceived well by the reviewers: Making the paper reproducible is important, regardless of whether the code and data are provided or not.
- If the contribution is a dataset and/or model, the authors should describe the steps taken to make their results reproducible or verifiable.
- Depending on the contribution, reproducibility can be accomplished in various ways. For example, if the contribution is a novel architecture, describing the architecture fully might suffice, or if the contribution is a specific model and empirical evaluation, it may be necessary to either make it possible for others to replicate the model with the same dataset, or provide access to the model. In general, releasing code and data is often one good way to accomplish this, but reproducibility can also be provided via detailed instructions for how to replicate the results, access to a hosted model (e.g., in the case of a large language model), releasing of a model checkpoint, or other means that are appropriate to the research performed.
- While NeurIPS does not require releasing code, the conference does require all submissions to provide some reasonable avenue for reproducibility, which may depend on the nature of the contribution. For example
 - (a) If the contribution is primarily a new algorithm, the paper should make it clear how to reproduce that algorithm.
 - (b) If the contribution is primarily a new model architecture, the paper should describe the architecture clearly and fully.
 - (c) If the contribution is a new model (e.g., a large language model), then there should either be a way to access this model for reproducing the results or a way to reproduce the model (e.g., with an open-source dataset or instructions for how to construct the dataset).
 - (d) We recognize that reproducibility may be tricky in some cases, in which case authors are welcome to describe the particular way they provide for reproducibility. In the case of closed-source models, it may be that access to the model is limited in

some way (e.g., to registered users), but it should be possible for other researchers to have some path to reproducing or verifying the results.

5. Open access to data and code

Question: Does the paper provide open access to the data and code, with sufficient instructions to faithfully reproduce the main experimental results, as described in supplemental material?

Answer: **[Yes]** The authors provide open access to their complete code with complete instructions to reproduce the results.

Justification: The authors provide the link to the dataset and the zip file for the complete code in the supplementary material as well as in the main paper during the time of submission.

Guidelines:

- The answer NA means that paper does not include experiments requiring code.
- Please see the NeurIPS code and data submission guidelines (<https://nips.cc/public/guides/CodeSubmissionPolicy>) for more details.
- While we encourage the release of code and data, we understand that this might not be possible, so “No” is an acceptable answer. Papers cannot be rejected simply for not including code, unless this is central to the contribution (e.g., for a new open-source benchmark).
- The instructions should contain the exact command and environment needed to run to reproduce the results. See the NeurIPS code and data submission guidelines (<https://nips.cc/public/guides/CodeSubmissionPolicy>) for more details.
- The authors should provide instructions on data access and preparation, including how to access the raw data, preprocessed data, intermediate data, and generated data, etc.
- The authors should provide scripts to reproduce all experimental results for the new proposed method and baselines. If only a subset of experiments are reproducible, they should state which ones are omitted from the script and why.
- At submission time, to preserve anonymity, the authors should release anonymized versions (if applicable).
- Providing as much information as possible in supplemental material (appended to the paper) is recommended, but including URLs to data and code is permitted.

6. Experimental setting/details

Question: Does the paper specify all the training and test details (e.g., data splits, hyperparameters, how they were chosen, type of optimizer, etc.) necessary to understand the results?

Answer: **[Yes]** The authors provide complete training and test details of the experimentation.

Justification: The complete details of the experimentation and dataset are provided in section 3 and Appendix section B of the paper.

Guidelines:

- The answer NA means that the paper does not include experiments.
- The experimental setting should be presented in the core of the paper to a level of detail that is necessary to appreciate the results and make sense of them.
- The full details can be provided either with the code, in Appendix, or as supplemental material.

7. Experiment statistical significance

Question: Does the paper report error bars suitably and correctly defined or other appropriate information about the statistical significance of the experiments?

Answer: **[Yes]** Yes, we do provide this information.

Justification: We do not explicitly provide this information as this is directly not relevant to our approach but do perform ablation studies in Appendix regarding different hyperparameter settings and the deviations/errors they can cause during train-test times.

Guidelines:

- The answer NA means that the paper does not include experiments.
- The authors should answer "Yes" if the results are accompanied by error bars, confidence intervals, or statistical significance tests, at least for the experiments that support the main claims of the paper.
- The factors of variability that the error bars are capturing should be clearly stated (for example, train/test split, initialization, random drawing of some parameter, or overall run with given experimental conditions).
- The method for calculating the error bars should be explained (closed form formula, call to a library function, bootstrap, etc.)
- The assumptions made should be given (e.g., Normally distributed errors).
- It should be clear whether the error bar is the standard deviation or the standard error of the mean.
- It is OK to report 1-sigma error bars, but one should state it. The authors should preferably report a 2-sigma error bar than state that they have a 96% CI, if the hypothesis of Normality of errors is not verified.
- For asymmetric distributions, the authors should be careful not to show in tables or figures symmetric error bars that would yield results that are out of range (e.g. negative error rates).
- If error bars are reported in tables or plots, The authors should explain in the text how they were calculated and reference the corresponding figures or tables in the text.

8. Experiments compute resources

Question: For each experiment, does the paper provide sufficient information on the computer resources (type of compute workers, memory, time of execution) needed to reproduce the experiments?

Answer: **[Yes]** The authors provide this information.

Justification: The authors have provided the exact hardware details and compute run times in section 3.

Guidelines:

- The answer NA means that the paper does not include experiments.
- The paper should indicate the type of compute workers CPU or GPU, internal cluster, or cloud provider, including relevant memory and storage.
- The paper should provide the amount of compute required for each of the individual experimental runs as well as estimate the total compute.
- The paper should disclose whether the full research project required more compute than the experiments reported in the paper (e.g., preliminary or failed experiments that didn't make it into the paper).

9. Code of ethics

Question: Does the research conducted in the paper conform, in every respect, with the NeurIPS Code of Ethics <https://neurips.cc/public/EthicsGuidelines>?

Answer: **[Yes]** It conforms in every aspect.

Justification: The dataset was entirely self-generated via a physics-based ray tracing pipeline using imported open-source 3D environment models and MATLAB's RayTracing object (no proprietary or sensitive data were used), and all code and data processing rely either on original implementations by the authors or publicly available open-source tools and libraries, fully respecting anonymity and the NeurIPS ethical guidelines

Guidelines:

- The answer NA means that the authors have not reviewed the NeurIPS Code of Ethics.
- If the authors answer No, they should explain the special circumstances that require a deviation from the Code of Ethics.
- The authors should make sure to preserve anonymity (e.g., if there is a special consideration due to laws or regulations in their jurisdiction).

10. Broader impacts

Question: Does the paper discuss both potential positive societal impacts and negative societal impacts of the work performed?

Answer: [Yes] The authors discuss this in their paper.

Justification: The authors discuss broader impacts in section 6.

Guidelines:

- The answer NA means that there is no societal impact of the work performed.
- If the authors answer NA or No, they should explain why their work has no societal impact or why the paper does not address societal impact.
- Examples of negative societal impacts include potential malicious or unintended uses (e.g., disinformation, generating fake profiles, surveillance), fairness considerations (e.g., deployment of technologies that could make decisions that unfairly impact specific groups), privacy considerations, and security considerations.
- The conference expects that many papers will be foundational research and not tied to particular applications, let alone deployments. However, if there is a direct path to any negative applications, the authors should point it out. For example, it is legitimate to point out that an improvement in the quality of generative models could be used to generate deepfakes for disinformation. On the other hand, it is not needed to point out that a generic algorithm for optimizing neural networks could enable people to train models that generate Deepfakes faster.
- The authors should consider possible harms that could arise when the technology is being used as intended and functioning correctly, harms that could arise when the technology is being used as intended but gives incorrect results, and harms following from (intentional or unintentional) misuse of the technology.
- If there are negative societal impacts, the authors could also discuss possible mitigation strategies (e.g., gated release of models, providing defenses in addition to attacks, mechanisms for monitoring misuse, mechanisms to monitor how a system learns from feedback over time, improving the efficiency and accessibility of ML).

11. Safeguards

Question: Does the paper describe safeguards that have been put in place for responsible release of data or models that have a high risk for misuse (e.g., pretrained language models, image generators, or scraped datasets)?

Answer: [No] There is no use of such models in the paper.

Justification: We do not use such models in this paper.

Guidelines:

- The answer NA means that the paper poses no such risks.
- Released models that have a high risk for misuse or dual-use should be released with necessary safeguards to allow for controlled use of the model, for example by requiring that users adhere to usage guidelines or restrictions to access the model or implementing safety filters.
- Datasets that have been scraped from the Internet could pose safety risks. The authors should describe how they avoided releasing unsafe images.
- We recognize that providing effective safeguards is challenging, and many papers do not require this, but we encourage authors to take this into account and make a best faith effort.

12. Licenses for existing assets

Question: Are the creators or original owners of assets (e.g., code, data, models), used in the paper, properly credited and are the license and terms of use explicitly mentioned and properly respected?

Answer: [Yes] The authors credit every asset owner that is used in this paper.

Justification: The authors fully credit the 3DGS and NeRF authors throughout the paper and they are available open source. Other than that no proprietary or scraped assets are used.

Guidelines:

- The answer NA means that the paper does not use existing assets.
- The authors should cite the original paper that produced the code package or dataset.
- The authors should state which version of the asset is used and, if possible, include a URL.
- The name of the license (e.g., CC-BY 4.0) should be included for each asset.
- For scraped data from a particular source (e.g., website), the copyright and terms of service of that source should be provided.
- If assets are released, the license, copyright information, and terms of use in the package should be provided. For popular datasets, paperswithcode.com/datasets has curated licenses for some datasets. Their licensing guide can help determine the license of a dataset.
- For existing datasets that are re-packaged, both the original license and the license of the derived asset (if it has changed) should be provided.
- If this information is not available online, the authors are encouraged to reach out to the asset's creators.

13. New assets

Question: Are new assets introduced in the paper well documented and is the documentation provided alongside the assets?

Answer: [Yes] New assets are introduced in the paper.

Justification: Yes, we provide complete details of the new dataset generation in section B as well as the novel Gaussian radial field construction explained in section 2

Guidelines:

- The answer NA means that the paper does not release new assets.
- Researchers should communicate the details of the dataset/code/model as part of their submissions via structured templates. This includes details about training, license, limitations, etc.
- The paper should discuss whether and how consent was obtained from people whose asset is used.
- At submission time, remember to anonymize your assets (if applicable). You can either create an anonymized URL or include an anonymized zip file.

14. Crowdsourcing and research with human subjects

Question: For crowdsourcing experiments and research with human subjects, does the paper include the full text of instructions given to participants and screenshots, if applicable, as well as details about compensation (if any)?

Answer: [NA]

Justification: N/A

Guidelines:

- The answer NA means that the paper does not involve crowdsourcing nor research with human subjects.
- Including this information in the supplemental material is fine, but if the main contribution of the paper involves human subjects, then as much detail as possible should be included in the main paper.
- According to the NeurIPS Code of Ethics, workers involved in data collection, curation, or other labor should be paid at least the minimum wage in the country of the data collector.

15. Institutional review board (IRB) approvals or equivalent for research with human subjects

Question: Does the paper describe potential risks incurred by study participants, whether such risks were disclosed to the subjects, and whether Institutional Review Board (IRB) approvals (or an equivalent approval/review based on the requirements of your country or institution) were obtained?

Answer: [NA]

Justification: N/A

Guidelines:

- The answer NA means that the paper does not involve crowdsourcing nor research with human subjects.
- Depending on the country in which research is conducted, IRB approval (or equivalent) may be required for any human subjects research. If you obtained IRB approval, you should clearly state this in the paper.
- We recognize that the procedures for this may vary significantly between institutions and locations, and we expect authors to adhere to the NeurIPS Code of Ethics and the guidelines for their institution.
- For initial submissions, do not include any information that would break anonymity (if applicable), such as the institution conducting the review.

16. Declaration of LLM usage

Question: Does the paper describe the usage of LLMs if it is an important, original, or non-standard component of the core methods in this research? Note that if the LLM is used only for writing, editing, or formatting purposes and does not impact the core methodology, scientific rigor, or originality of the research, declaration is not required.

Answer: [Yes]

Justification: LLMs were only used for formatting and grammatical corrections in the paper.

Guidelines:

- The answer NA means that the core method development in this research does not involve LLMs as any important, original, or non-standard components.
- Please refer to our LLM policy (<https://neurips.cc/Conferences/2025/LLM>) for what should or should not be described.